Accepted Manuscript

Rate-dependent phase-field damage modeling of rubber and its experimental parameter identification

Pascal J. Loew, Bernhard Peters, Lars A.A. Beex

PII: S0022-5096(18)31043-3
DOI: https://doi.org/10.1016/j.jmps.2019.03.022
Reference: MPS 3597

To appear in: *Journal of the Mechanics and Physics of Solids*

Received date: 6 December 2018
Revised date: 24 February 2019
Accepted date: 29 March 2019

Please cite this article as: Pascal J. Loew, Bernhard Peters, Lars A.A. Beex, Rate-dependent phase-field damage modeling of rubber and its experimental parameter identification, *Journal of the Mechanics and Physics of Solids* (2019), doi: https://doi.org/10.1016/j.jmps.2019.03.022

Rate-dependent phase-field damage modeling of rubber and its experimental parameter identification

Pascal J. Loew[a,b,*], Bernhard Peters[a], Lars A.A. Beex[a]

[a] *Faculté des Sciences, de la Technologie et de la Communication, Université du Luxembourg*
[b] *SISTO Armaturen S.A., Echternach*

Abstract

Phase-field models have the advantage in that no geometric descriptions of cracks are required, which means that crack coalescence and branching can be treated without additional effort. Miehe et al. [1] introduced a rate-independent phase-field damage model for finite strains in which a viscous damage regularization was proposed. We extend the model to depend on the loading rate and time by incorporating rubber's strain-rate dependency in the constitutive description of the bulk, as well as in the damage driving force. The parameters of the model are identified using experiments at different strain rates. Local strain fields near the crack tip, obtained with digital image correlation (DIC), are used to help identify the length scale parameter. Three different degradation functions are assessed for their accuracy to model the rubber's rate-dependent fracture. An adaptive time-stepping approach with a corrector scheme is furthermore employed to increase the computational efficiency with a factor of six, whereas an active set method guarantees the irreversibility of damage. Results detailing the energy storage and dissipation of the different model constituents are included, as well as validation results that show promising capabilities of rate-dependent phase-field modeling.

Keywords: Phase-field, fracture, damage, rubber, rate-dependent

*Corresponding author
Email address: `loew.pascal@gmail.com` (Pascal J. Loew)

1. Introduction

Rubber products like seals, hoses and tires are widely used in industrial applications. In order to reduce the cost and time constraints to produce physical prototypes, virtual prototypes can be developed instead. However, virtual prototypes require adequate numerical simulation tools to describe the mechanical responses. Several researchers have modeled the failure and fracture of rubber materials [1] [2] [3], but rubber's rate-dependency is still relatively scarcely addressed.

Although [4], [5] and [6] have recognized the viscoelastic behavior as a major factor affecting the crack growth rate, to the best of the authors' knowledge, only [7] and [8] have incorporated it in predictive models with a node splitting algorithm and a cohesive zone approach, respectively. These approaches have a disadvantage in that they need either frequent remeshing or a-priori knowledge of the crack path.

Phase-field damage models for fracture [9], also called variational approaches to fracture [10], are recently gaining interest since they naturally manage crack propagation, branching and coalescence without a-priori knowledge of the crack path. This is achieved by treating the sharp discontinuity in a continuous manner with a finite damage zone that is governed by a length scale parameter. The similarities to gradient-enhanced damage models [11] [12] [13] [14] [15] are obvious and highlighted in [16] and [17].

[1] was, according to the best of the authors' knowledge, the first to introduce phase-field modeling for fracture of rubbery polymers. While already including rate-dependency in the damage evolution, its aim was to add numerical stability to the framework. An extension to anisotropic, hyperelastic materials, like soft biological tissues, was presented in [18] and [19]. [20] and [21] used a phase-field damage model to investigate the failure at the microscale of carbon black reinforced rubber composites. These works highlighted the ability of phase-field damage approaches to model nucleation and coalescence of several cracks. The fracture of silicone elastomers was studied in [2], whereas [3] introduced a mi-

cromechanically motivated definition of the crack driving force in a phase-field approach for loosely crosslinked rubbery polymers. Evaluating various failure criteria for soft biological materials, [22] favored a strain-energy based criterion to describe damage evolution, which we use as well.

Phase-field approaches for fracture need a correct identification of the length scale parameter. It can be shown that for an infinitesimally small length scale the approach converges to a sharp crack surface [9]. This could lead to the assumption that the length scale is a numerical parameter, which just needs to be selected small enough. However, a substantial influence of the length scale on the results is observed in [23]. Therefore we assume, as in [24], [25], [26], and [27], that the length scale is a material parameter depending on the microstructure and needs to be calibrated with experimental data.

Although the general aim of this work is to develop a phase-field model to describe the rate-dependent failure of rubbers, four sub-aims can be distinguished. First, we extend the proposed model of [1] to incorporate rate-dependency in the bulk response as well as in the damage evolution. Second, since enforcing the irreversibility of the damage field by the application of a local history field [9] yields erroneous results for the rate-dependent formulation, we propose to directly use the constraints on the evolution of the damage field. Third, we introduce an adaptive time-stepping algorithm and use the corrector scheme of [28] to reduce computation times. Fourth, [29] showed for a gradient-enhanced damage model, that measurements of local strains near the crack tip are required to correctly calibrate the fracture parameters, especially the length scale. We experimentally identify all material parameters, including the length scale, such that the computations for the presented validation tests are true predictions.

The paper is organized as follows. In chapter 2, the rate-dependent phase-field damage model for finite strains is derived from energy-conservation. In chapter 3, we formulate the weak form, linearize and discretize our model. Special attention is paid to the treatment of the irreversibility constraint of the damage field. Chapter 4 presents the conducted experiments, the procedure to identify the model's parameters and the validation results. We discuss amongst other things the value of the length scale parameter for which we have used digital image correlation (DIC) measurements and assess three different degradation functions in terms of accuracy to predict failure of rubber. The validation is performed by varying the specimen geometries and clamp velocities. We conclude this contribution in chapter 5.

In this work, we denote scalars by lowercase and capital letters (a and A), vectors by bold, lowercase letters ($\mathbf{a}$), second-order tensors by bold capitals ($\mathbf{A}$) and fourth-order tensors by bold, capital italic letters ($\boldsymbol{\mathcal{A}}$).

2. Energy-based rate-dependent phase-field damage model

In this section, the rate-dependent phase-field damage model is derived. We start by defining the kinematics. We consider a body Ω_0 in the reference configuration, with its external boundary denoted by $\partial\Omega_0$ and an internal discontinuity Γ_0. The motion and deformation of the body are described by displacement $\mathbf{u}$, deformation gradient $\mathbf{F} = \mathbf{I} + \nabla_0\mathbf{u}$ and Green's strain tensor $\mathbf{E} = 1/2(\mathbf{F}^T \cdot \mathbf{F} - \mathbf{I})$. $\mathbf{I}$ denotes the unit tensor and spatial derivatives associated with the reference configuration are denoted by $\frac{\partial \cdot}{\partial \mathbf{X}} = \nabla_0(\cdot)$. Further, we introduce a scalar-valued phase-field damage variable $d \in [0,1]$ such that $d = 0$ for an undamaged, virgin material and $d = 1$ for a fully damaged, degraded material (See figure 2.1a).

Energy conservation requires the externally supplied energy per time unit $\dot{P}^{ext}$, to be equal to the rate of the internally stored $\dot{E}$ and the dissipated energy $\dot{D}$:

$$\dot{E} + \dot{D} = \dot{P}^{ext}. \tag{2.1}$$

The respective relations for $\dot{E}$, $\dot{D}$ and $\dot{P}^{ext}$ are defined in the following subsections. By inserting these relations in equation (2.1), we can derive the governing equations for our model.

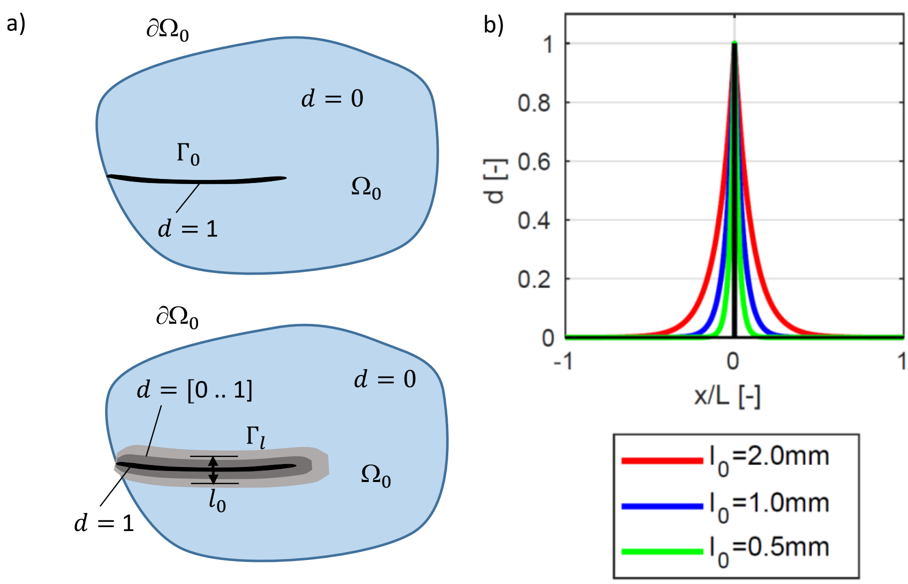

Figure 2.1: a) In a 2-D phase-field damage model a sharp crack Γ_0 is approximated with crack surface Γ_l. b) Damage variable d for a fully developed crack in a 1-D bar with length L. The width of the process zone is controlled by the length scale l_0.

2.1. Rate of internally stored energy

The internally stored energy in the bulk reads:

$$E = \int_{\Omega_0 \backslash \Gamma_0} \psi^{bulk} dV = \int_{\Omega_0} g_d \psi^{bulk} dV, \tag{2.2}$$

where we have introduced the degradation function g_d [1], which controls the stiffness of the bulk material as a function of the damage variable d. The degradation function obeys:

$$\begin{aligned} g_d(d = 0) &= 1 \\ g_d(d = 1) &= 0 \\ \left.\frac{\partial g_d}{\partial d}\right|_{d=1} &= 0. \end{aligned} \tag{2.3}$$

Most studies (e.g. [9], [19],[21], [30]) use the following quadratic degradation function:

$$g_d = (1-d)^2. \tag{2.4}$$

In contrast, [31] recently introduced the following degradation function:

$$g_d = s\left((1-d)^3 - (1-d)^2\right) + 3(1-d)^2 - 2(1-d)^3, \tag{2.5}$$

where $s > 0$ is an additional parameter, which needs to be calibrated. This degradation function reduces the growth of the damage variable d prior to the critical stress. For details on the influence of the parameter s, the reader is also referred to [16]. In chapter 4.4 we investigate the influence of the degradation function in more detail. As in [31], we set $s = 10^{-4}$.

To incorporate rate-dependent effects, we split the strain energy density into an elastic ψ^{elas} and viscous contribution ψ^{visc}:

$$\psi^{bulk} = \psi^{elas}(\mathbf{F}) + \psi^{visc}(\mathbf{F}, \mathbf{\Phi}_\alpha). \tag{2.6}$$

$\mathbf{\Phi}_\alpha$ denotes an internal strain-like tensor, that accounts for the dissipation in the bulk. It is actually the 3D extension of the 1D strain γ_α in a dashpot of a Maxwell element (see figure 2.2).

Considering the incompressibility of rubbery polymers, the elastic strain energy density is normally decomposed in an isochoric and volumetric part according

[1]Note that we do not add a small constant c to the degradation function ($g_d = g_d + c$), as it is for example employed in [2],[3] or [9], to ensure the stability of the resulting system of equations. The reason is that even a small value for c in combination with a higher order hyperelastic material model has an influence on the solution. Therefore we use an additional Neo-Hookean strain energy potential $\psi^{res} = C_1^{res}(tr(\mathbf{F}^T \cdot \mathbf{F}) - 3)$ in parallel to the elastic ψ^{elas} and viscous ψ^{vis}. This potential does not decline with the degradation function g_d, but the value $C_1^{res} = 5 \cdot 10^{-3} MPa$ is selected so small that it has no influence on the results (not shown here). To present the model as simply as possible we do not include ψ^{res} in the following equations.

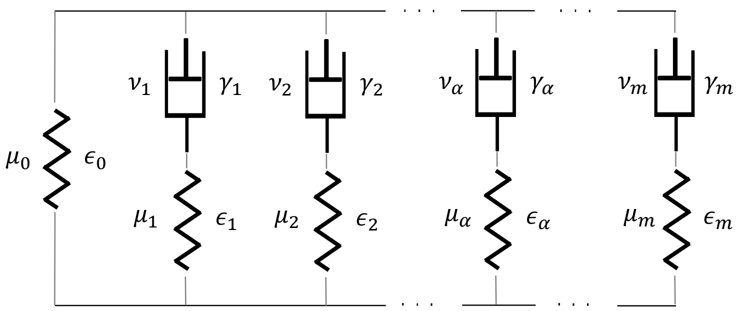

Figure 2.2: Generalized Maxwell-element with m spring-dashpot elements. While μ_α and ϵ_α denote the stiffness and strain in the spring, ν_α and γ_α denote the viscosity and the strain in the dashpot.

to:

$$\psi^{elas} = \psi^{iso}(\bar{\mathbf{F}}) + \psi^{vol}(J), \tag{2.7}$$

where $\bar{\mathbf{F}} = J^{-1/3}\mathbf{F}$ and $J = det(\mathbf{F})$. In this contribution, however, we only consider plane stress cases. With that, the incompressibility constraint can be applied via substitution in the out of plane deformation [32]. Therefore, we obtain with $J = 1$ [2]:

$$\psi^{elas} = \psi^{iso}(\mathbf{F}). \tag{2.8}$$

The rate of the internally stored energy then reads:

$$\dot{E} = \int_{\Omega_0} \left(g_d \frac{\partial \psi^{bulk}}{\partial \mathbf{F}} : \dot{\mathbf{F}} + g_d \sum_{\alpha=1}^{m} \frac{\partial \psi^{bulk}}{\partial \mathbf{\Phi}_\alpha} : \dot{\mathbf{\Phi}}_\alpha + \frac{\partial g_d}{\partial d} \psi^{bulk} \dot{d} \right) dV. \tag{2.9}$$

[2] It is known to the authors, that rubbers do not deform in a perfectly incompressible way ([33], [34]). Recently, researches [35] have shown that decohesion of filler particles from the elastomer matrix is the main reason for the volume growth in tension. With this knowledge, one could postulate a coupling of the compressibility and volume growth to the field of the damage variable. For the sake of simplicity, this is not done in this study and remains an open point for the future.

2.1.1. Constitutive equations for the bulk

For the elastic part ψ^{elas} we use the strain energy density of a reduced polynomial model [36], which reads:

$$\psi^{elas} = \sum_{i=1}^{3} C_i (I_1 - 3)^i, \tag{2.10}$$

where C_i denote material parameters and $I_1 = tr(\mathbf{F}^T \cdot \mathbf{F})$.

Next, we define the viscous contribution $\psi_\alpha^{visc}(\mathbf{F}, \mathbf{\Phi}_\alpha)$ with the model for linear viscosity, but finite strains from [37].[3] This model is a 3-D generalization of the 1-D generalized Maxwell model (figure 2.2) with the viscous stress

$$q_\alpha = \mu_\alpha(\epsilon_0 - \gamma_\alpha) = \nu_\alpha \dot{\gamma}_\alpha. \tag{2.11}$$

Since the energy density ψ^{bulk} is split into an elastic and a viscous term, the same applies to the first Piola-Kirchhoff stress:

$$\begin{aligned} \mathbf{P} = \frac{\partial \psi}{\partial \mathbf{F}} &= g_d \frac{\partial \psi^{bulk}}{\partial \mathbf{F}} \\ &= g_d \left(\frac{\partial \psi^{elas}}{\partial \mathbf{F}} + \sum_{\alpha=1}^{m} \frac{\partial \psi_\alpha^{vis}}{\partial \mathbf{F}} \right) \\ &= g_d \left(\mathbf{P}^\infty + \sum_{\alpha=1}^{m} \mathbf{Q}_\alpha \right), \end{aligned} \tag{2.12}$$

where

$$\mathbf{P}^\infty = 2 \sum_{i=1}^{3} i \; C_i (I_1 - 3)^{(i-1)} \; \mathbf{F}. \tag{2.13}$$

$\mathbf{Q}_\alpha$ denotes the non-equilibrium stress, while $\mathbf{P}^\infty$ denotes the time-infinity stress. From the Clausius-Planck inequality, we extract the rate of dissipation

[3] There are other, more sophisticated viscoelastic material models for rubber, for example [38], [39] or [40], but these models require an internal Newton-scheme to more accurately account for the viscosity. These models come with substantially larger computational costs. In chapter 4 we show that the model of [37] is accurate enough for our application.

of the bulk as:

$$\dot{D}^{visc} = -g_d \sum_{\alpha=1}^{m} \frac{\partial \psi_\alpha^{vis}}{\partial \mathbf{\Phi}_\alpha} : \dot{\mathbf{\Phi}}_\alpha = g_d \sum_{\alpha=1}^{m} \mathbf{Q}_\alpha : \dot{\mathbf{\Phi}}_\alpha \geq 0, \tag{2.14}$$

where we have introduced:

$$\mathbf{Q}_\alpha = -\frac{\partial \psi_\alpha^{vis}}{\partial \mathbf{\Phi}_\alpha} \ . \tag{2.15}$$

The constraint on the viscous rate of dissipation in equation (2.14) is satisfied by defining the following evolution law for the internal strain-like variables

$$\dot{\mathbf{\Phi}}_\alpha = \boldsymbol{\mathcal{V}} : \mathbf{Q}_\alpha, \tag{2.16}$$

where $\boldsymbol{\mathcal{V}}$ denotes a positive definite fourth order tensor containing the inverse viscosity. Incorporating the time derivative of equation (2.11), we formulate the evolution equation within the one-dimensional and linear regime:

$$\dot{q}_\alpha + \frac{\mu_\alpha}{\nu_\alpha} q_\alpha = \dot{\overline{\mu_\alpha \epsilon_0}}. \tag{2.17}$$

Motivated by the solution of the one-dimensional example (equation (2.17)), the viscoelastic stress $\mathbf{Q}_a$ is calculated via the following rate equation:[4]

$$\dot{\mathbf{Q}}_\alpha + \frac{\mathbf{Q}_\alpha}{\tau_\alpha} = \dot{\mathbf{P}}_\alpha, \tag{2.18}$$

where τ_α denotes the relaxation time of the α^{th} spring-dashpot element in the 3-D generalized Maxwell model. Assuming that the elastic and viscoelastic bulk consist of identical polymer chains, relationship $\psi_\alpha = \beta_\alpha^\infty \psi^{elas}$ is introduced so that:

$$\mathbf{P}_\alpha = \frac{\partial \psi_\alpha}{\partial \mathbf{F}} = \beta_\alpha^\infty \frac{\partial \psi^{elas}}{\partial \mathbf{F}} = \beta_\alpha^\infty \mathbf{P}^\infty. \tag{2.19}$$

[4] The viscous response of the material model according to [37] is calculated solely with the rate equation (2.18) and its numerical solution (2.21). Therefore, the model does not require the explicit definition of the fourth order tensor $\boldsymbol{\mathcal{V}}$ and the viscous energy density ψ^{visc}. For the one-dimensional case however, we write $\psi_\alpha^{visc} = \frac{1}{2}\mu_\alpha(\epsilon_0 - \gamma_\alpha)^2$ so that $q_\alpha = \frac{\partial \psi_\alpha^{visc}}{\partial \epsilon_0} = -\frac{\partial \psi_\alpha^{visc}}{\partial \gamma_\alpha} = \mu_\alpha(\epsilon_0 - \gamma_\alpha)$. This justifies equation (2.15) and comparing equations (2.11) and (2.16), we deduce that $\boldsymbol{\mathcal{V}}$ is the three-dimensional extension of ν_α^{-1}.

β_α^∞ denote scalar free energy factors. A closed-form solution of rate equation (2.18) for the time interval $t \in [0, T]$ can be expressed by convolution integrals as follows:

$$\mathbf{Q}_\alpha = e^{-\frac{T}{\tau_\alpha}} \mathbf{Q}_{\alpha,0} + \int_{t=0}^{t=T} e^{-\frac{T-t}{\tau_\alpha}} \dot{\mathbf{P}}_\alpha dt, \tag{2.20}$$

where $\mathbf{Q}_{\alpha,0}$ denotes the instantaneous response. Applying a second-order accurate mid-point rule for the time integration, the viscous stress for the current time step can then be expressed as:

$$\mathbf{Q}_\alpha = e^{2\zeta_\alpha} \mathbf{Q}_{\alpha,n} + e^{\zeta_\alpha} \beta_\alpha^\infty \left(\mathbf{P}^\infty - \mathbf{P}_n^\infty \right), \tag{2.21}$$

where $\zeta = \frac{-\Delta t}{2\tau_\alpha}$ and subscripts n denotes converged solutions of the previous time step t_n.

2.2. Rate of Dissipation

Additional to the viscous rate of dissipation in the bulk (equation (2.14)), we introduce dissipation due to crack growth. Following the pioneering work of [41] and especially [6] for elastomers, we use an energetic approach to fracture. First, we define G_c as the energy dissipated by the formation of a unit crack area. Thus, the energy dissipated trough crack formation reads:

$$D^{crack} = \int_{\Gamma_0} G_c \; dA. \tag{2.22}$$

Integrating over the fractured surface Γ_0 is difficult and would require constant remeshing or sophisticated enrichment strategies like XFEM [42]. To circumvent this surface integral, we approximate the fractured surface $\Gamma_0 \approx \Gamma_l = \int_{\Omega_0} \gamma_l \; dV$ [10]. With the crack density function $\gamma_l = \gamma_l(d)$, the sharp discontinuity of the crack is smoothened out to a diffuse topology. The size of this zone is controlled by the length scale parameter l_0 (See figure 2.1 b). Multiplying G_c with γ_l and integrating over the domain Ω_0, the dissipated energy trough crack formation now reads:

$$D^{crack} = \int_{\Gamma_0} G_c \; dA = \int_{\Omega_0} G_c \gamma_l \; dV. \tag{2.23}$$

As in [9] and [10], we set the crack density function to [5]:

$$\gamma_l = \frac{1}{2l_0} d^2 + \frac{l_0}{2} \left(\nabla_0 d \cdot \nabla_0 d \right), \tag{2.24}$$

so that the dissipation rate due to crack formation can be written as:

$$\dot{D}^{crack} = \int_{\Omega_0} G_c \left(\frac{1}{l_0} d\dot{d} + l_0 \nabla_0 d \cdot \nabla_0 \dot{d} \right) dV. \tag{2.25}$$

Integration by parts and use of the divergence theorem then yields:

$$\dot{D}^{crack} = \int_{\Omega_0} G_c \left(\frac{1}{l_0} d - l_0 \nabla_0^2 d \right) \dot{d} \; dV + \int_{\partial\Omega_0} G_c l_0 \nabla_0 d \cdot \mathbf{n}_0 \; \dot{d} \; dA. \tag{2.26}$$

$\mathbf{n}_0$ denotes the outward, unit normal vector and we introduce rate-dependent crack growth dissipation as follows: [6]

$$\dot{D}^{crack,visc} = \int_{\Omega_0} \kappa_1 \dot{d}^2 \; dV, \tag{2.27}$$

where scalar κ_1 denotes a viscosity parameter.

The total rate of dissipation consequently reads:

$$\dot{D} = \dot{D}^{crack} + \dot{D}^{crack,visc} + \dot{D}^{visc} \geq 0. \tag{2.28}$$

Enforcing $\dot{d} \geq 0$ (see chapter 3.4) implies that $\dot{D}^{crack} \geq 0$ and hence, that cracks cannot heal. Constraint $\dot{D}^{visc} \geq 0$ was discussed in chapter 2.1.1 and more details can be found in [37]. A positive value of κ_1 finally ensures that $\dot{D}^{crack,visc} \geq 0$.

[5] Alternatively, [43] introduced another crack density function: $\gamma_l = \frac{3}{8l_0} d + \frac{3l_0}{8} \left(\nabla_0 d \cdot \nabla_0 d \right)$. This function leads in combination with the quadratic degradation function $g_d = (1-d)^2$ to a reduction of the growth of damage variable d prior to the critical stress [27]. We can reproduce this behavior with the crack density (equation (2.24)) and the degradation function as in equation (2.5). Therefore, we have decided to keep the crack density function constant and only vary the degradation function (see chapter 4.4)

[6] One could introduce higher order viscosity terms with $\kappa_\beta \dot{d}^{2\beta}$ with $\beta > 1$. However, this hardly changes the solution. To keep the model as simple as possible, we set $\beta = 1$.

2.3. Rate of externally applied energy

The rate of externally applied energy reads:

$$\dot{P}^{ext} = \int_{\partial\Omega_0} \mathbf{t}_0 \cdot \dot{\mathbf{u}} \; dA + \int_{\Omega_0} \mathbf{b}_0 \cdot \dot{\mathbf{u}} \; dV, \tag{2.29}$$

where $\mathbf{t}_0$ and $\mathbf{b}_0$ denote the surface traction and the volumetric body force vector, respectively.

2.4. Balance of mechanical energy

Inserting equations (2.9), (2.28) and (2.29) into equation (2.1) we obtain

$$\begin{aligned}
&-\int_{\Omega_0} \left(\nabla_0 \cdot \left(g_d \frac{\partial \psi^{bulk}}{\partial \mathbf{F}} \right) + \mathbf{b}_0 \right) \cdot \dot{\mathbf{u}} \; dV + \int_{\partial\Omega_0} \left(g_d \frac{\partial \psi^{bulk}}{\partial \mathbf{F}} \cdot \mathbf{n}_0 - \mathbf{t}_0 \right) \cdot \dot{\mathbf{u}} \; dA \\
&+ \int_{\Omega_0} \left(\frac{\partial g_d}{\partial d} \psi^{bulk} + \frac{G_c}{l_0} d - G_c l_0 \nabla_0^2 d + \kappa_1 \dot{d} \right) \dot{d} \; dV \\
&+ \int_{\partial\Omega_0} G_c l_0 \nabla_0 d \cdot \mathbf{n}_0 \dot{d} \; dA + \int_{\Omega_0} \sum_{\alpha=1}^{m} g_d \left(\mathbf{Q}_\alpha + \frac{\partial \psi^{bulk}}{\partial \mathbf{\Phi}_\alpha} \right) : \dot{\mathbf{\Phi}}_\alpha \; dV = 0.
\end{aligned} \tag{2.30}$$

From this, we can extract the macroforce[7]:

$$\nabla_0 \cdot \left(g_d \frac{\partial \psi^{bulk}}{\partial \mathbf{F}} \right) + \mathbf{b}_0 = 0, \tag{2.31}$$

and the microforce balance:

$$\frac{\partial g_d}{\partial d} \psi^{bulk} + \frac{G_c}{l_0} d - G_c l_0 \nabla_0^2 d + \kappa_1 \dot{d} = 0. \tag{2.32}$$

We want to point out, that equation (2.32) contains a viscous regularization of the damage growth $\kappa_1 \dot{d}$, as well as a rate-dependent driving force:

$$\psi^{bulk} = \psi^{elas} + \psi^{visc} = \int \mathbf{P}^\infty : \dot{\mathbf{F}} dt \; + \; \sum_{\alpha=1} \int \mathbf{Q}_\alpha : \dot{\mathbf{F}} dt. \tag{2.33}$$

Finally, the following Neumann boundary conditions may be applied:

$$g_d \frac{\partial \psi^{bulk}}{\partial \mathbf{F}} \cdot \mathbf{n}_0 = \mathbf{t}_0 \;\; \text{and} \;\; \nabla_0 d \cdot \mathbf{n}_0 = 0. \tag{2.34}$$

3. Numerical Implementation

3.1. Weak form

Next, we transform the macroforce balance (equation (2.31)) and microforce balance (equation (2.32)) to their respective weak form using the standard Galerkin procedure with the test functions $\delta\mathbf{u}$ and δd.

We obtain the macroforce balance in the weak form:

$$R_u = \int_{\Omega_0} \mathbf{P} : \nabla_0 \delta\mathbf{u} \; dV - \int_{\Omega_0} \mathbf{b}_0 \cdot \delta\mathbf{u} \; dV - \int_{\Gamma_0} \mathbf{t}_0 \cdot \delta\mathbf{u} \; dS = 0. \tag{3.1}$$

Application of the Galerkin procedures to the microforce balance leads to:

$$R_d = \int_{\Omega_0} \left(G_c l_0 \nabla_0^2 d \; \delta d - \frac{\partial g_d}{\partial d} \psi^{bulk} \; \delta d - \frac{G_c}{l_0} d \; \delta d - \kappa_1 \dot{d} \; \delta d \right) dV = 0. \tag{3.2}$$

After integration by parts and use of the boundary condition $\nabla_0 d \cdot \boldsymbol{n}_0 = 0$, equation (3.2) reads:

$$R_d = \int_{\Omega_0} \left(G_c l_0 \nabla_0 d \cdot \nabla_0 \delta d + \frac{\partial g_d}{\partial d} \psi^{bulk} \; \delta d + \frac{G_c}{l_0} d \; \delta d + \kappa_1 \dot{d} \; \delta d \right) dV = 0. \tag{3.3}$$

With degradation function $g_d = (1-d)^2$ and denoting $\eta_1 = \frac{l_0}{G_c}\kappa_1$, we obtain:

$$\begin{aligned} R_d = & \int_{\Omega_0} \left(l_0^2 \nabla_0 d \cdot \nabla_0 \delta d \right) dV + \\ & \int_{\Omega_0} \left(-2(1-d)\psi^{bulk} \frac{l_0}{G_c} + d + \eta_1 \dot{d} \right) \delta d \; dV = 0. \end{aligned} \tag{3.4}$$

[7] By multiplying the stress tensor $\mathbf{P} = g_d \frac{\partial \psi^{bulk}}{\partial \mathbf{F}}$ with the degradation function g_d in equation (2.31), we degenerate the complete bulk response. In case of cyclic loading, this leads to the problem that crack closure is not described correctly. Further, one can see from equation (2.32) that the complete bulk energy is responsible for crack growth, independent of compressive or tensile deformation. As shown in [44], this might lead to an erroneous result in compression. To account for crack surface contacts and to allow crack growth to originate only from tensile deformation, a split of the bulk energy into a positive (tensile) and negative (compression) part is introduced in [44]: $\psi^{bulk} = g_d \psi^+ + \psi^-$. The reader is also referred to [45], in which a spectral decomposition of the strain tensor is used to split the strain energy density into a positive and negative part. Focusing for now on examples that are only exposed to tension, we simplify the model and do not split the energy.

Finally, we deduce from equation (3.1) and (3.4) two coupled equations:

$$
\begin{aligned}
R_u &= R_u(\delta\mathbf{u}, \mathbf{u}, d) = 0 \\
R_d &= R_d(\delta d, \mathbf{u}, d, \dot{d}) = 0,
\end{aligned}
\tag{3.5}
$$

which we need to solve.

3.2. Linearization

To solve equation (3.1) and (3.4), we first discretize the problem in time using a backward Euler scheme:

$$
\dot{d} = \frac{d - d_n}{\Delta t}, \tag{3.6}
$$

resulting in $R_d = R_d(\delta d, \mathbf{u}, d, d_n)$, where d_n denotes the solution of the damage field for previous time step t_n.

We then apply a staggered scheme as in [9] and perform an operator split into a mechanical predictor step $ALGO_M$ and damage growth step $ALGO_D$. Accordingly, we solve equation (3.1) at time t_{n+1} for the displacement field $\mathbf{u}$, while keeping the damage field d constant:

$$
ALGO_M = \begin{cases} R_u = 0 \\ \dot{d} = 0. \end{cases} \tag{3.7}
$$

Then, with the updated, but constant displacement field $\mathbf{u}$, we solve equation (3.4) for the damage field d:

$$
ALGO_D = \begin{cases} \dot{\mathbf{u}} = 0 \\ R_d = 0. \end{cases} \tag{3.8}
$$

Each equation is solved with the Newton-Raphson method. To do so, we need to linearise both equations:

$$
\begin{aligned}
R_u + \left.\frac{\partial R_u}{\partial \mathbf{u}}\right|_{\mathbf{u},d} \cdot \Delta\mathbf{u} = 0 \\
R_d + \left.\frac{\partial R_d}{\partial d}\right|_{\mathbf{u},d} \Delta d = 0.
\end{aligned}
\tag{3.9}
$$

Note that the directional derivatives $\left.\frac{\partial R_u}{\partial d}\right|_{\mathbf{u},d}$ and $\left.\frac{\partial R_d}{\partial \mathbf{u}}\right|_{\mathbf{u},d}$ are neglected. It is shown in [9] that this scheme is more stable and faster than the monolithic approach with a full linearization. The only disadvantage is that a sufficiently small time step is required [46].

Calculating the directional derivative for R_u, we obtain:

$$\left.\frac{\partial R_u}{\partial \mathbf{u}}\right|_{\mathbf{u},d} \cdot \Delta\mathbf{u} = \int_{\Omega_0} g_d \left(1 + \sum_{\alpha=1}^{m} e^{\zeta_\alpha} \beta_\alpha\right) \nabla_0 \delta\mathbf{u} : \boldsymbol{\mathcal{C}}^\infty : \nabla_0 \Delta\mathbf{u}\, dV, \tag{3.10}$$

where

$$\boldsymbol{\mathcal{C}}^\infty = \frac{\partial \mathbf{P}^\infty}{\partial \mathbf{F}} = 2 \sum_{i=1}^{3} i\, C_i (I_1 - 3)^{i-1}\, \boldsymbol{\mathcal{I}} + 2i\,(i-1)\, C_i (I_1 - 3)^{i-2}\, \mathbf{F} \otimes \mathbf{F}. \tag{3.11}$$

Herein, $\otimes$ denotes a dyadic product and $\boldsymbol{\mathcal{I}} = \delta_{ik}\delta_{jl}\, \mathbf{e}_i \otimes \mathbf{e}_j \otimes \mathbf{e}_k \otimes \mathbf{e}_l$. The directional derivative for R_d furthermore reads:

$$\begin{aligned} \left.\frac{\partial R_d}{\partial d}\right|_{\mathbf{u},d} \Delta d = &\int_{\Omega_0} l_0^2 \nabla_0 \delta d \cdot \nabla_0 \Delta d\, dV \\ &+ \int_{\Omega_0} \delta d \left(2\psi^{bulk} \frac{l_0}{G_c} + 1 + \eta_1 \frac{1}{\Delta t}\right) \Delta d\, dV. \end{aligned} \tag{3.12}$$

3.3. Discretization

The spatial discretization of the domain is achieved with linear, isoparametric quadrilaterals. Using N_a to denote the shape function of the a^{th} node and n_{nodes} to denote the number of nodes, the displacement field $\mathbf{u}$ and the damage field d are approximated as:

$$\begin{aligned} \mathbf{u} &= \sum_{a=1}^{n_{nodes}} N_a \mathbf{u}_a, \\ d &= \sum_{a=1}^{n_{nodes}} N_a d_a. \end{aligned} \tag{3.13}$$

Including these approximations in the weak form, we write:

$$\begin{aligned} R_u(\mathbf{u}, d) + \left.\frac{\partial R_u}{\partial \mathbf{u}}\right|_{\mathbf{u},d} \cdot \Delta\mathbf{u} &= \delta\underline{\mathbf{u}} \cdot \left(\underline{\mathbf{f}}^u + \underline{\underline{\mathbf{K}}}^{uu} \cdot \Delta\underline{\mathbf{u}}\right) = 0 \\ R_d(\mathbf{u}, d) + \left.\frac{\partial R_d}{\partial d}\right|_{\mathbf{u},d} \Delta d &= \delta\underline{d} \left(\underline{f}^d + \underline{\underline{K}}^{dd} \Delta\underline{d}\right) = 0, \end{aligned} \tag{3.14}$$

where a single bar under a variable denotes a column and a double bar under a variable denotes a matrix. Since both equations must hold true for all possible variations of the displacement field and damage field, we can write the final nonlinear system of equations as follows:

$$\begin{aligned} \underline{\mathbf{f}}^u + \underline{\underline{\mathbf{K}}}^{uu} \cdot \Delta\underline{\mathbf{u}} &= \underline{\mathbf{0}} \\ \underline{f}^d + \underline{\underline{K}}^{dd} \Delta\underline{d} &= \underline{0}, \end{aligned} \tag{3.15}$$

where

$$\begin{aligned} \underline{\mathbf{f}}^u &= f^u_{ia} = \int_{\Omega_0} \frac{\partial N_a}{\partial X_j} P_{ij}\, dV - \int_{\Omega} N_a b_{0,i}\, dV - \int_{\Gamma} N_a t_{0,i}\, dS, \\ \underline{f}^d &= f^d_a = \int_{\Omega_0} l_0^2\, \frac{\partial N_b d_b}{\partial X_j}\, \frac{\partial N_a}{\partial X_j} dV + \\ &\int_{\Omega_0} N_a \left(-2(1 - N_b d_b)\psi^{bulk} \frac{l_0}{G_c} + N_b d_b\; + \eta_1 N_b \frac{d_b - d_{n,b}}{\Delta t} \right)\, dV, \\ \underline{\underline{\mathbf{K}}}^{uu} &= [K^{uu}_{ab}]_{ik} = \int_{\Omega_0} g_d \left(1 + \sum_{\alpha=1}^{m} e^{\zeta_\alpha} \beta_\alpha \right) \frac{\partial N_a}{\partial X_j}\, \mathcal{C}^{\infty}_{ijkl}\, \frac{\partial N_b}{\partial X_l}\, dV, \\ \underline{\underline{K}}^{dd} &= [K^{uu}_{ab}] = \int_{\Omega_0} l_0^2\, \frac{\partial N_a}{\partial X_i}\, \frac{\partial N_b}{\partial X_i}\, dV \\ &+ \int_{\Omega_0} N_a \left(2\psi^{bulk} \frac{l_0}{G_c} + 1 + \frac{\eta_1}{\Delta t} \right) N_b\, dV. \end{aligned} \tag{3.16}$$

3.4. Enforcing Irreversibility with an Active Set Method

It is essential that damaged material is prevented from healing. We examine this problem for a 1D rate-dependent formulation without gradient terms [23]. Equation (2.32) then reads with $g_d = (1-d)^2$:

$$2(1-d)\psi^{bulk} - \frac{G_c}{l_0} d - \kappa_1 \dot{d} = 0. \tag{3.17}$$

Furthermore, we assume a linear-elastic material $\psi^{bulk} = \frac{1}{2}E\epsilon^2$, where E and ϵ denote the Young's modulus and the strain, respectively. Inserting $\dot{d} = \frac{d-d_n}{\Delta t}$, we obtain the following damage variable at the end of the current time step:

$$d = \frac{2\psi^{bulk} + \frac{\kappa_1 d_n}{\Delta t}}{2\psi^{bulk} + \frac{G_c}{l_0} + \frac{\kappa_1}{\Delta t}}. \tag{3.18}$$

If we now apply strains as depicted in figure 3.1a), we would observe healing for a decrease of the strain, until the material is entirely healed at $\epsilon_{(t=4s)} = 0$. To avoid healing (i.e. to guarantee irreversibility of the damage), [9] introduced the following history variable:

$$H = \max_{s=[0,t]} \left[\psi^{bulk}(s) \right] , \tag{3.19}$$

such that equation (3.18) reads:

$$d = \frac{2H + \frac{\kappa_1 d_n}{\Delta t}}{2H + \frac{G_c}{l_0} + \frac{\kappa_1}{\Delta t}} . \tag{3.20}$$

The results are presented in figure 3.1b) - d). Even though history variable H remains constant for a decrease of the strain, damage variable d continues to grow. Therefore, instead of using the history variable H, we use an active set method [47] to enforce $\dot{d} \geq 0$ as a constraint (as in [48]).

The part of the system of equations associated with the computation of the damage variable is partitioned into a set $\mathcal{A} = \{i | d < d_n\}$ with active constraints and with complementary inactive constraint $\mathcal{I}$. Within each Newton iteration, we solve the reduced system of the inactive constraint as follows:

$$\Delta \underline{d}_{\mathcal{I}} = - \left(\underline{\underline{K}}^{dd} \right)^{-1}_{\mathcal{I}\mathcal{I}} \underline{f}^{d}_{\mathcal{I}} , \tag{3.21}$$

while setting $\Delta \underline{d}_{\mathcal{A}} = 0$. The active set $\mathcal{A}$ is updated within each iteration until the constraint is fulfilled at every node. The procedure is detailed in the pseudo-code presented in algorithm 1. As can be seen in figure 3.1, the damage stops growing for a decreasing strain using this method.

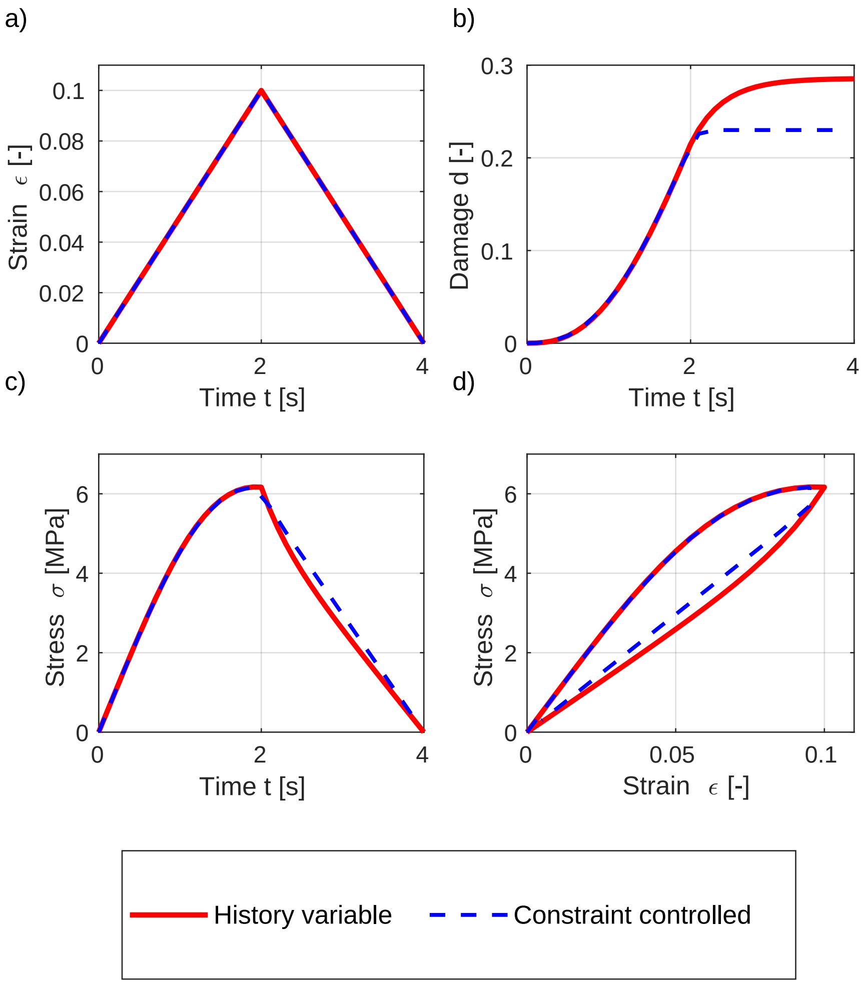

Figure 3.1: Solutions of a rate-dependent 1-D phase-field model calculated with a history field and a constraint on $\dot{d}$ a) Applied strain over time b) Evolution of the damage variable over time c) Evolution of the stress over time d) Strain-stress response of the system.

Algorithm 1 Active Set Newton Method

$\mathcal{A} = \emptyset,\ \mathcal{I} = all$

while $Res > tol$ **do**

  Assemble $\underline{f}^d, \underline{\underline{K}}^{dd} \leftarrow \underline{\mathbf{u}}, \underline{d}^{k-1}, \underline{d}_n$

  $Res = ||\mathbf{f}^d_{\mathcal{I}}||$

  $\Delta \underline{d}^k_{\mathcal{I}} = -\left(\underline{\underline{K}}^{dd}\right)^{-1}_{\mathcal{I}\mathcal{I}} \underline{f}^d_{\mathcal{I}}$

  while $\Delta \underline{d}_{\mathcal{I}} < 0$ **do**

    $\mathcal{A} = \mathcal{A} \cup (\Delta \underline{d}_{\mathcal{I}} < 0)$

    $\Delta \underline{d}_{\mathcal{A}} = 0$

    $\mathcal{I} = \mathcal{I} \cap \mathcal{A}$

    $\Delta \underline{d}^k_{\mathcal{I}} = -\left(\underline{\underline{K}}^{dd}\right)^{-1}_{\mathcal{I}\mathcal{I}} \underline{f}^d_{\mathcal{I}}$

  $\underline{d}^k = \underline{d}^{k-1} + \Delta \underline{d}^k$

  $k = k + 1$

Return

3.5. Corrector scheme and time adaptivity

As detailed in chapter 3.2, equations (3.1) and (3.4) are solved in the staggered scheme as proposed by [9]. A disadvantage of this approach is a need of a sufficiently small time step. To decrease the calculation time we introduce adaptive time stepping. This reduces or increases the time step depending on the growth of the damage variable from one converged time step to another.

Furthermore, we have incorporated a corrector scheme according to [28] with iterations between the macro- and microforce balance within one time step. This means that for each time step we solve first for the displacements $\underline{\mathbf{u}}^j$ and then for the damage field $\underline{d}^j$, but instead of proceeding to the next time step, we calculate again the displacement field $\underline{\mathbf{u}}^{j+1}$ with the updated damage field $\underline{d}^j$. Next, we update damage field $\underline{d}^{j+1}$. The scheme only proceeds to the next time step if the change of the displacement field and damage field from one iteration to the other is smaller than a predefined tolerance. The pseudo code for this scheme is presented in algorithm 2, where Δt_{min} and Δt_{max} denote the limits for the time step size. Note that $ALGO_D$ is solved with the active-set method as outlined in algorithm 1.

To highlight the advantage of the scheme, we compare in figure 3.2 the global force response of a single-edge notched tensile test for different time steps. Details of the geometry can be found in figure 4.1a), while the fracture parameters are set to $l_0 = 1.50mm$, $G_c = 3.0N/mm$ and $\eta_1 = \frac{l_0}{G_c}\kappa_1 = 0.05$. Further, we set $\Delta t_{max} = 50\Delta t_{min}$ and $tol_3 = 5.0 \cdot 10^{-4}$. The staggered scheme converges for a sufficiently small time step Δt_{min} to a stable solution. By applying the corrector scheme, we can use a substantially larger time step. In combination with the time step adaptivity, the calculation time is approximately reduced by a factor of 6. Note that we did not use the time step adaptivity for the first three results, but did the simulation with $\Delta t = \Delta t_{max}$ until $\lambda = 1.05$ and then $\Delta t = \Delta t_{min}$. Therefore, the time step adaptivity not only reduces the computation time but also the required user input, since the timing of the time step change depends on each case.

Algorithm 2 Corrector scheme + time step adaptivity

```
$\underline{\mathbf{u}}^0 = \underline{\mathbf{u}}^1 = \underline{\mathbf{u}}^2 = \underline{\mathbf{u}}_n$
$\underline{d}^0 = \underline{d}^1 = \underline{d}^2 = \underline{d}_n$
$j = 2$
while ($Res_1 > tol_1$ or $Res_2 > tol_2$) do
    solve $ALGO_M\left(\underline{\mathbf{u}}^{j-1}, \underline{d}^{j-1}\right)$ for $\underline{\mathbf{u}}^j$
    solve $ALGO_D\left(\underline{\mathbf{u}}^{j}, \underline{d}^{j-1}\right)$ for $\underline{d}^j$
    $Res_1 = \frac{abs(||\underline{d}^{j-1}-\underline{d}^{j-2}|| - ||\underline{d}^{j}-\underline{d}^{j-1}||)}{1+||\underline{d}^{j-1}-\underline{d}^{j-2}||}$
    $Res_2 = \frac{abs(||\underline{\mathbf{u}}^{j-1}-\underline{\mathbf{u}}^{j-2}|| - ||\underline{\mathbf{u}}^{j}-\underline{\mathbf{u}}^{j-1}||)}{1+||\underline{\mathbf{u}}^{j-1}-\underline{\mathbf{u}}^{j-2}||}$
    $j = j + 1$
if $max(\underline{d}^j - \underline{d}_n) > tol_3$ then
    $\Delta t = max(\Delta t_n/2; \Delta t_{min})$
else
    $\Delta t = min(1.2\Delta t_n; \Delta t_{max})$
$t = t_n + \Delta t$
$\underline{\mathbf{u}} = \underline{\mathbf{u}}^j$
$\underline{d} = \underline{d}^j$
Return
```

ACCEPTED MANUSCRIPT

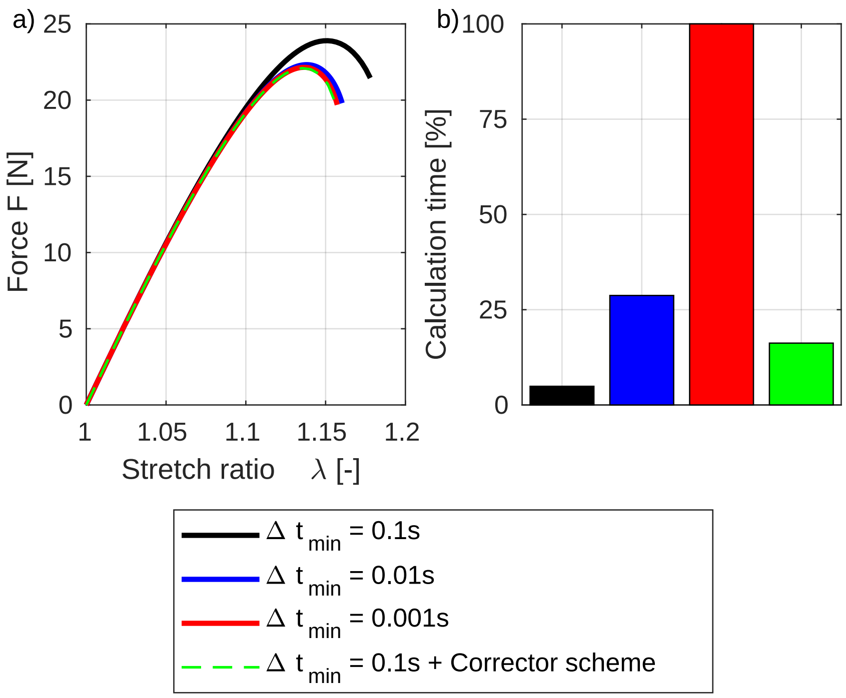

Figure 3.2: a) Force to stretch-ratio response for various time steps for a single notch tensile test. The solution converges for a sufficiently small time step. b) Normalized calculation time for various time steps.

4. Results

We start this chapter by introducing the experiments used to identify the material parameters. Next, we discuss the influence of the degradation function. Length scale l_0 as a material parameter is set to a finite size and we argue that the value obtained from our experiments fits the material microstructure. Last, we validate the model with the identified parameter set by performing additional numerical tests and compare the results to their experimental counterparts.

4.1. Experiments

An ethylene propylene diene monomer rubber (EPDM) is tested in all experiments, which are of a plane stress nature. The strains are measured using a laser extensometer and we also use digital image correlation (DIC) to measure strain fields. Because crack growth in EPDM is highly dependent on temperature, we have conducted all experiments at a constant temperature of $20°C$.

First, the bulk parameters are identified using uniaxial tensile tests, which are performed according to ISO 37:2002 with dumbbell specimens. The sample thickness is $2mm$, while the length is $20mm$ and the width is $4mm$. The results for three clamp velocities are presented in figure 4.2. We indeed observe that an increase in the loading rate yields larger stresses.

Single (SENT) and double-edge notch tensile tests (DENT) are performed to identify the phase-field parameters (see figure 4.1). Additionally to the force-displacement response, we can measure local strains near the crack tip using DIC. Due to the specifications of the camera, we only measure local strain fields during the SENT test for a clamp velocity of $25mm/min$. Local strain fields are computed using GOM Correlate software [49].

4.2. Identification of bulk material parameters

First, we calibrate the bulk material parameters. We use the hyperelastic model of [36] with three parameters according to equation (2.10) in combination with two Maxwell-elements [37]. The bulk parameters are identified using the least-squares method for which the minimization is performed using the Nelder-Mead

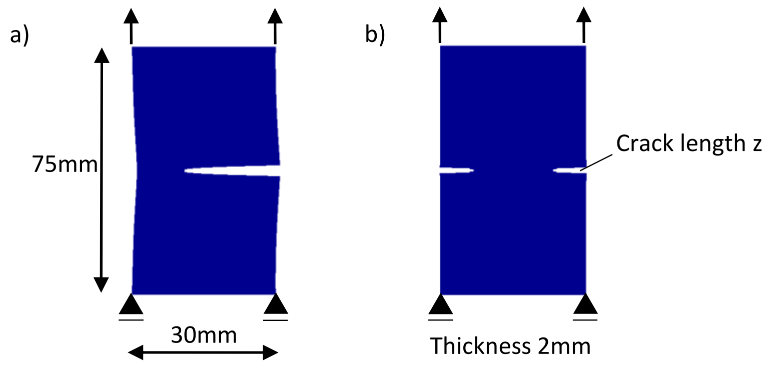

Figure 4.1: a) Single-edge notch tensile (SENT) test with crack length $z = 20mm$ b) Double-edge notch tensile (DENT) test with variable crack length z.

simplex approach in MATLAB [50]. Table 4.1 and figure 4.2 display the bulk parameters and the associated material responses, respectively.

Table 4.1: Identified material parameters for visco-hyperelastic model.

C_1 $[MPa]$	C_2 $[MPa]$	C_2 $[MPa]$
0.9600	0.0430	$6.316 * 10^{-06}$

β_1 $[-]$	β_2 $[-]$	τ_1 $[s]$	τ_2 $[s]$
0.40642	0.0284	4.9776	449.3075

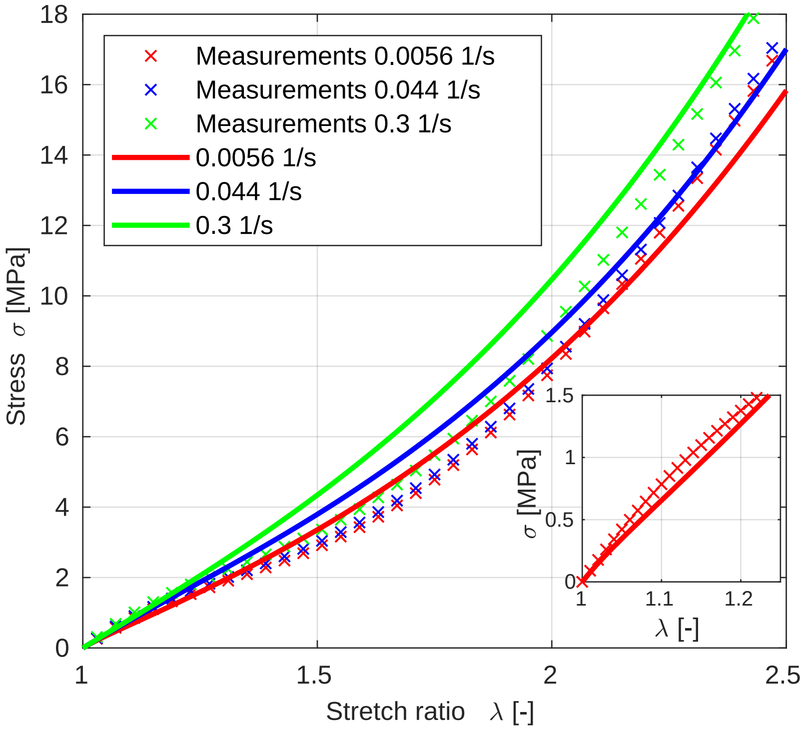

Figure 4.2: Uniaxial tensile test results: Averaged experimental results and material model responses for 3 clamp velocities after the bulk parameters are identified. All tests are performed at 20°C and at least 5 samples were tested per clamp velocity. The zoom in the right-bottom corner shows the result for a clamp velocity of $0.0056s^{-1}$.

4.3. Identification of phase-field damage parameters

The fracture parameters are identified using the force-displacement response of the SENT tests (figure 4.1) with an initial crack length of $20mm$ and the DENT test with an initial crack of $7mm$. Measurements are recorded during the SENT tests with clamp velocities of $25mm/min$ (test data $y_{k,25mes}$) and $200mm/min$ ($y_{k,200mes}$) and during the DENT test with a clamp velocity of $75mm/min$ ($y_{k,75mes}$). Lastly, we include the local strains in front of the crack tip measured via DIC ($y_{k,25mesDIC}$). The local strains are measured at a global displacement of $10.5mm$, which is the point of crack nucleation in our experiments. By application of the least squares method, we define the residual to be minimized:

$$\begin{aligned} RES = w\Bigg(\sum_{k=1}^{n_{mes25}} \left(\frac{y_{k,25mes} - y_{k,25}}{y_{k,25mes}} \right)^2 + \sum_{k=1}^{n_{mes200}} \left(\frac{y_{k,200mes} - y_{k,200}}{y_{k,200mes}} \right)^2 \\ + \sum_{k=1}^{n_{mes75}} \left(\frac{y_{k,75mes} - y_{k,75}}{y_{k,75mes}} \right)^2 \Bigg) \\ + (1-w) \sum_{k=1}^{n_{mes25DIC}} \left(\frac{y_{k,25mesDIC} - y_{k,25DIC}}{y_{k,25mesDIC}} \right)^2, \end{aligned} \tag{4.1}$$

where subscript mes denotes experimentally measured values. The scalar $w = 0.25$ is introduced to weigh the force-displacement results with respect to the measured local strains. The minimization of the residual is performed using a genetic algorithm [51] and the identified fracture parameters are presented in table 4.2.

Table 4.2: Identified fracture parameters for degradation function $g_{d,1} = (1-d)^2$.

G_c $[N/mm]$	l_0 $[mm]$	η_1 $[-]$
7.819	0.55040	0.10610

4.3.1. Single-edge notch tensile tests

In this subsection, we show the experimental and numerical results of the cases used to calibrate the fracture parameters. The results for the DENT test with an initial crack $z = 7mm$ and a clamp velocity of $75mm/min$ ($y_{k,75mes}$) are presented in section 4.7.1 (figure 4.14b).

The evolution of the phase-field parameter d and therefore the crack propagation for the SENT test is shown in figure 4.3. By omitting elements with an average damage variable $d_{average} > 0.95$, the crack is made visible.

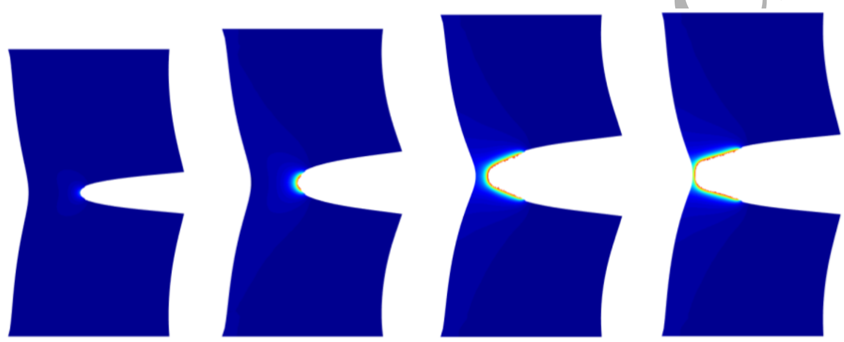

Figure 4.3: SENT test with initial crack size $z = 20mm$ and clamp velocity $25mm/min$: Numerically predicted crack growth over stretch ratio λ.

Next, we compare the force to stretch ratio response for a clamp velocity of $25mm/min$ and $200mm/min$. As can be seen in figure 4.4, the model is clearly capable of tracking the increase of the maximum tearing force for an increase of the clamp velocity.[8]

The experimental results for both velocities are compared to the numerical results in figure 4.5 and we observe a sufficiently accurate agreement.

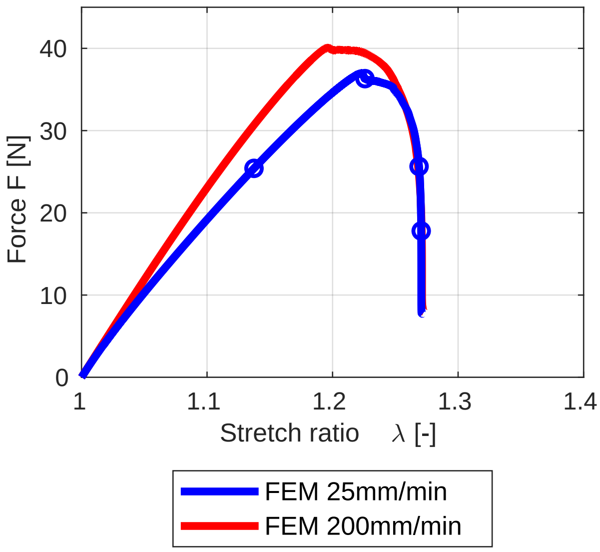

Figure 4.4: SENT test: Tearing force to stretch ratio for loading rates $25mm/min$ and $200mm/min$. The circles highlight the specific points at which we plot the damage variable in figure 4.3.

By application of the DIC technology, we were able to measure local strains near the crack tip. In figure 4.6 we compare the strains in the y-direction at a

[8]We see for both velocities a small kink in the force response after reaching the maximum tearing force. This kink is not observed in our experiments (figure 4.5). By tweaking our material parameters we could design a smooth force response. In detail, we could either increase the length-scale l_0, reduce the fracture toughness G_c, use a Neo-Hookean hyperelastic material model, or increase or decrease rate-dependency (η_1, τ_α, β_α). To the best of the authors' knowledge, this problem has not been reported before. [20] and [52] have investigated a SENT specimen with a higher-order hyperelastic material model [53] and rate-independent phase-field damage model. However, this kink was not occurring close to the maximum tearing force, but at a later stage, and they did not comment on it. We decide not to tweak the material parameters and postpone an investigation to a later work.

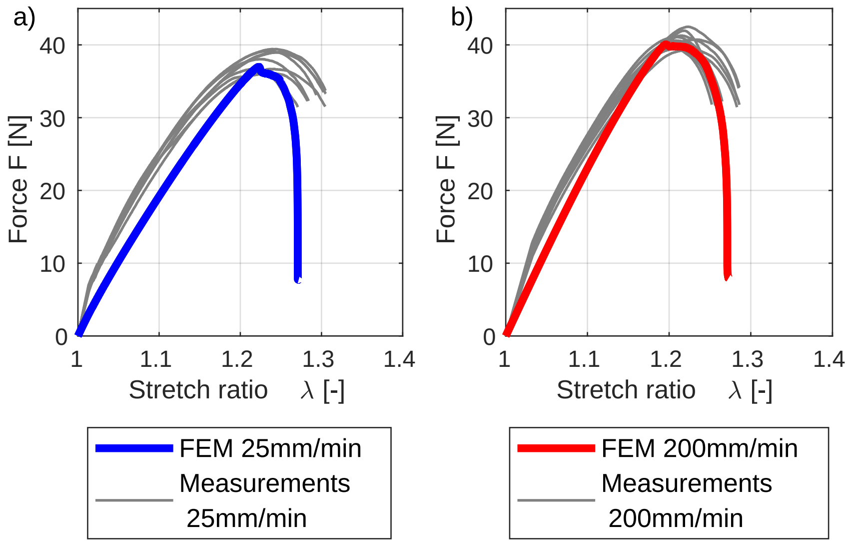

Figure 4.5: SENT test: Numerical and experimental results a) Force to stretch-ratio response for $25mm/min$. b) Force to stretch-ratio response for $200mm/min$.

global displacement of $10.5mm$. To better quantify the results we look at two paths, denoted by x and y in figure 4.6. The experimental and numerical results of these paths are plotted in figure 4.7. Comparing the size of the process zone, id est the region of large deformation, the accurate fit supports our identified value of the length scale parameter.

4.4. Influence of degradation function g_d

As shown in [54] and [55], the degradation function impacts the results and may be tailored to fit experimental measurements. Therefore, we also investigate the responses for the following two degradation functions: $g_{d,2} = (1-d)^3$ and $g_{d,3} = m[(1-d)^3-(1-d)^2]+3(1-d)^2-2(1-d)^3$. These degradation functions, together with the quadratic degradation function $g_{d,1} = (1-d)^2$, are presented in figure 4.8a). The cubic degradation function makes the damage grow faster than the original quadratic degradation function and the combined one makes the damage grow slower. Figure 4.8b) shows the material responses of a 1D

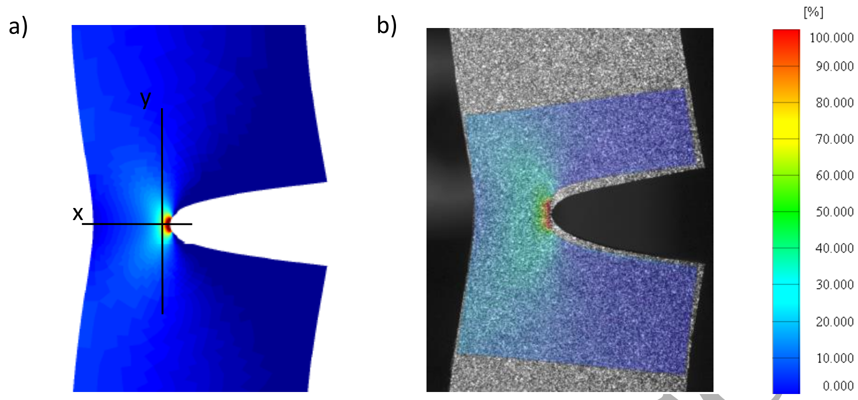

Figure 4.6: a) Numerically predicted Green-Strain Eyy. The lines x and y indicate the path along which we plot in figure 4.7 the strains. Additionally, the y-direction is corresponding with the y-path. b) Green-Strain Eyy measured via DIC.

bar with Young's modulus $E = 2000MPa$, length-scale $l_0 = 0.1mm$, viscosity $\kappa_1 = 0$ and fracture toughness $G_c = 2N/mm$. The combined quadratic, cubic degradation function clearly results in a nearly linear-elastic behavior before the onset of failure. The failure response itself is substantially more brittle than for the two other degradation functions. The responses for the other two degradation functions show that the onset of failure does not correspond to the maximum stress. The cubic degradation function furthermore results in a more ductile response than the quadratic one.

The identified fracture parameters for the degradation functions $g_{d,2}$ and $g_{d,3}$ are summarized in tables 4.3 and 4.4, respectively. Since the residual with the quadratic degradation function is the smallest, which is graphically illustrated for the SENT test at $25mm/min$ in figure 4.9, we select the quadratic one. For the interested reader, we have included the results for degradation functions $g_{d,2}$ and $g_{d,3}$ for the SENT test at $200mm/min$ and for the DENT tests in Appendix A.

Interestingly, we observe that the length scale parameter is of the same order of magnitude for all degradation functions ($l_0 \approx 0.55mm$). This strengthens the theory that the length scale parameter is indeed a parameter that depends on

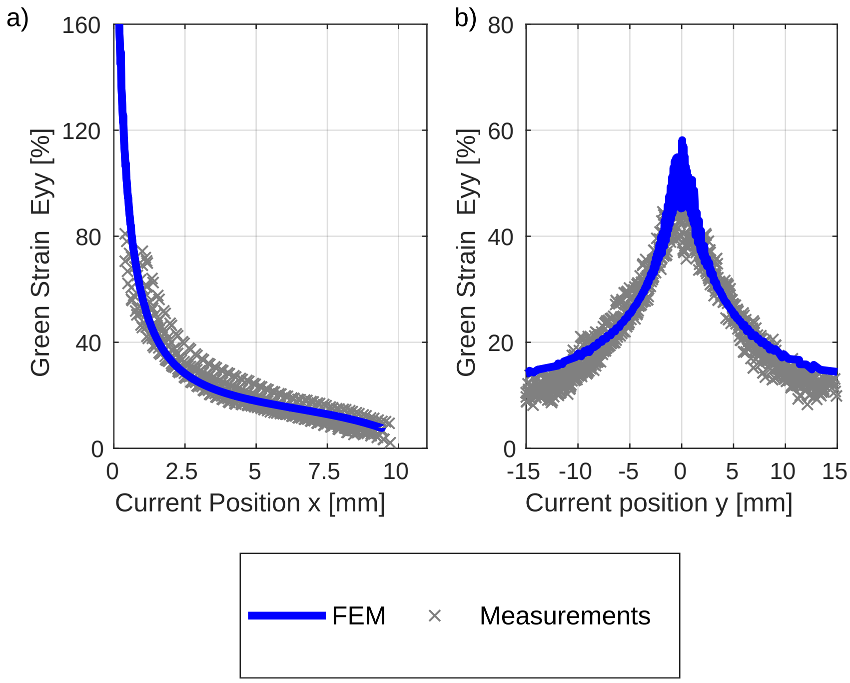

Figure 4.7: Comparison of experimental and numerical local Green-Strain Eyy: a) Local strains for path x b) Local strains for path y.

374 the microstructure of the material.

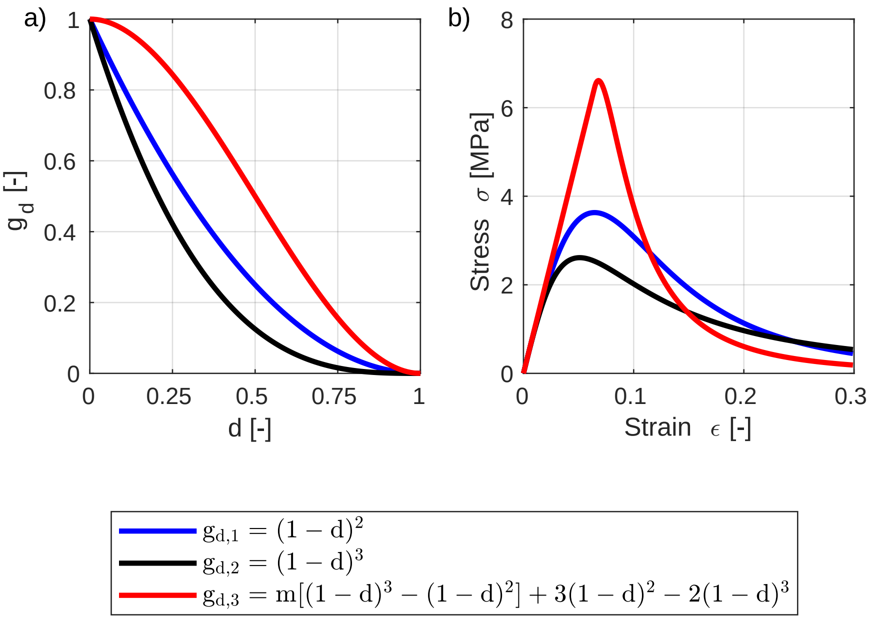

Figure 4.8: a) Evolution of the degradation functions for damage variable $d \in [0, 1]$ b) Stress-strain response for a linear elastic 1D case.

Table 4.3: Identified fracture parameters for degradation function $g_{d,2} = (1 - d)^3$.

G_c $[N/mm]$	l_0 $[mm]$	η_1 $[-]$
12.31	0.564	0.0766

Table 4.4: Identified fracture parameters for degradation function $g_{d,3} = m[(1 - d)^3 - (1 - d)^2] + 3(1 - d)^2 - 2(1 - d)^3$.

G_c $[N/mm]$	l_0 $[mm]$	η_1 $[-]$
4.426	0.693	0.0651

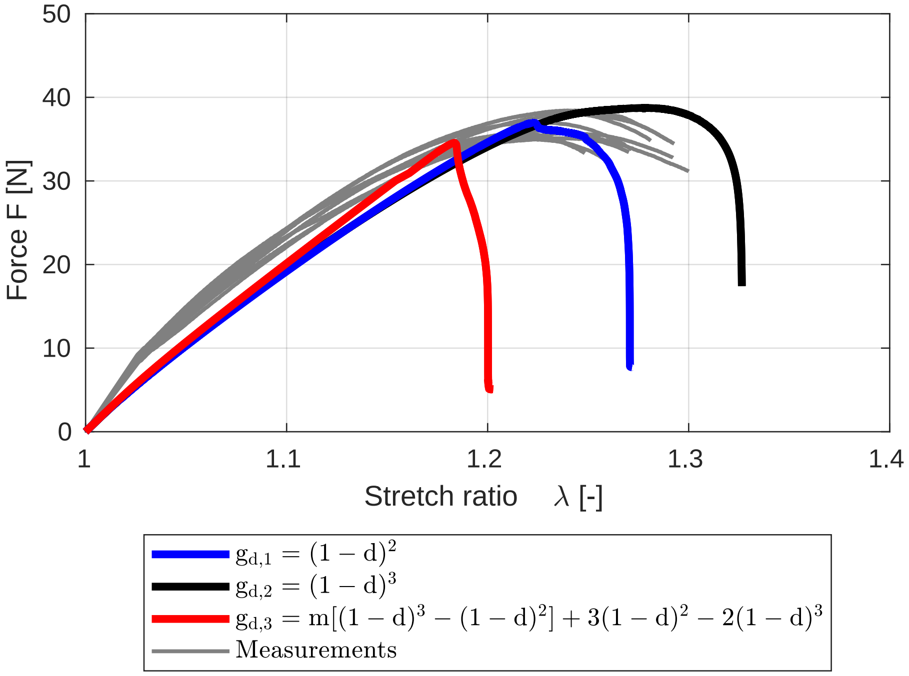

Figure 4.9: SENT responses ($25mm/min$) for the three degradation functions together with the experimental data.

4.5. Interpretation of length scale l_0

Optimization with genetic algorithm leads to a length scale parameter $l_0 = 0.55mm$. First, to validate that the length scale is not a solution of the grid size, we study in figure 4.10 the influence of the spatial discretization on the results. We see that the maximum force, as well as the local strains, do not depend on the mesh.

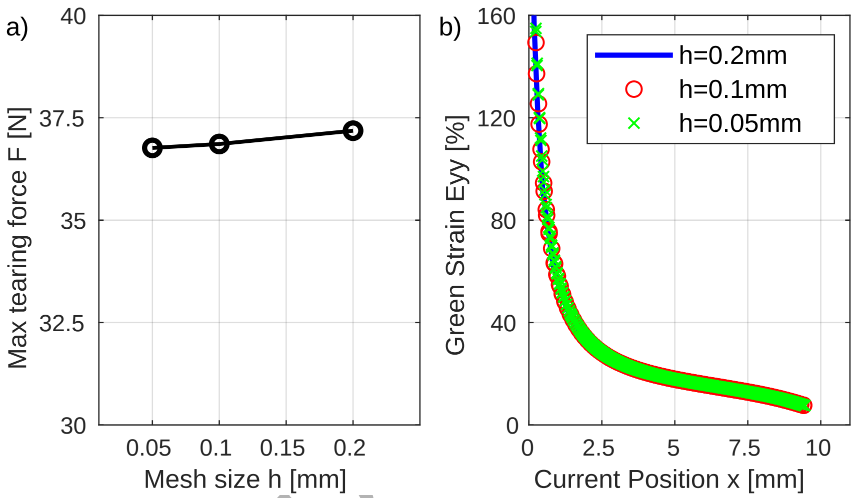

Figure 4.10: SENT test $25mm/min$: Comparison of three different mesh sizes h: a) Maximum tearing force b) Local strains Eyy for path x.

The EPDM rubber we use is reinforced with carbon particles. Consequently, we consider the microstructure of the rubber as a composite made of a polymer matrix and rigid carbon particles. Applying a high strain to this composite, debonding of the polymer matrix from the particles was observed [35]. We assume that the high local strains in front of the crack tip lead to debonding in a finite region. The resulting microcracks are then quantified in our model with a growth of the damage variable d (figure 4.11).

The average diameter of carbon particle agglomerates in our rubber is $15\mu m$, but they can be as large as $50\mu m$. Estimating that debonding occurs at several agglomerates in parallel, we argue that a length scale parameter of $0.55mm$ is

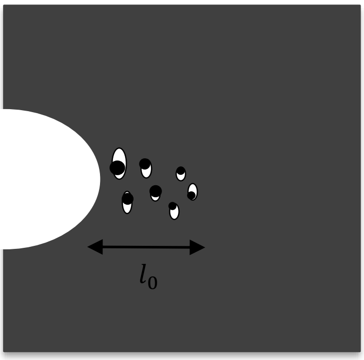

Figure 4.11: Due to many small inclusions, we expect debonding and subsequently microcracks to occur at a finite distance to the crack tip.

reasonable.

For comparison, [56] has predicted the characteristic length of damage localization in a natural rubber to be $0.2mm$. Measuring the heat source at the crack tip for a filled styrene-butadiene rubber (SBR) under cyclic loading a localization in a zone of 0.44 x $0.32mm^2$ is found in [57]. By assuming that the heat is generated by the formation of microcracks our argument of a finite process zone is strengthened. Tests on a filled SBR are also performed in [58]. Nanocavitation was observed by an X-ray microbeam scan and was found to be at least $300\mu m$ in front of the crack tip. Due to the fact that all these references have presented measured length scales of a similar magnitude for rubbers, the identified value can indeed be considered as appropriate.

4.6. Balance of mechanical energy and dissipation during crack growth

To verify the thermodynamical consistency of the model, id est the fulfillment of the first (2.1) and second law of thermodynamics (2.28), the energetic signature of the SENT test is shown in figure 4.12 for a clamp velocity of $25mm/min$ and in figure 4.13 for $200mm/min$. The maximum relative error of the external power and the sum of the internally stored and dissipated energy is

$err_{25} = max\left(\frac{\sum(E+D)-P^{ext}}{P^{ext}}\right) = 0.0052$ for $25mm/min$ and $err_{200} = 0.0022$ for $200mm/min$. Since the error is small, we consider the balance of mechanical energy fulfilled.

Note that we are only able to calculate the sum:

$$D^{visc} + E^{visc} = g_d \sum_{\alpha=1} \int \mathbf{Q}_\alpha : \dot{\mathbf{F}} dt, \tag{4.2}$$

because the material model of [37] does not include a split of the deformation tensor into an elastic and inelastic part. For clamp velocity $200mm/min$, a slight decrease of the sum $D^{visc}+E^{visc}$ is observed after reaching the maximum tearing force. D^{visc} can be seen as the dissipated energy in the dashpot (see figure 2.2), while E^{visc} is the stored energy in the spring in series to the dashpot. Especially for fast loading, such as $200mm/min$, the dashpot has no time to relax so that the energy stored in the spring is high. Therefore, we conclude that sum $D^{visc} + E^{visc}$ decreases due to the degradation of E^{visc} while $\dot{D}^{visc} \geq 0$. Since dissipation due to crack growth (D^{crack} and $D^{visc,crack}$) is increasing for the entire loading process, the second law of thermodynamics is fulfilled.

Further, we want to highlight that most of the viscous dissipation is caused by the bulk D^{visc}, and not by viscous crack resistance $D^{visc,crack}$. This shows the necessity to not only include the time and rate-dependency in the damage evolution, but also in the constitutive bulk response.

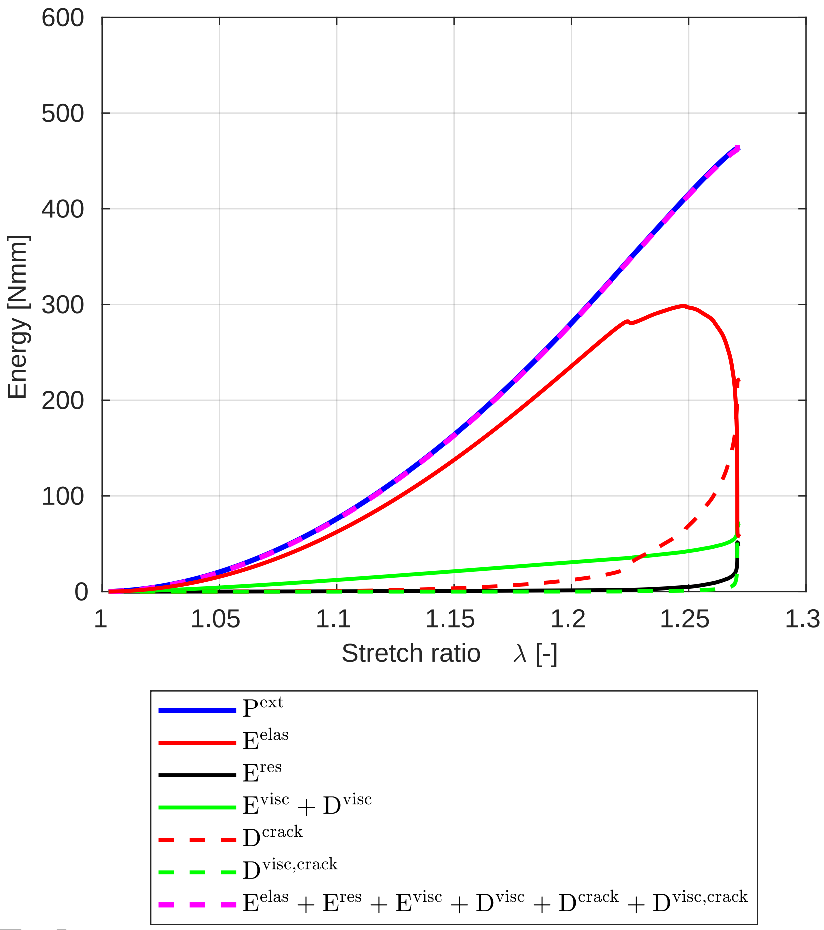

Figure 4.12: SENT test $25mm/min$: Energy of the system

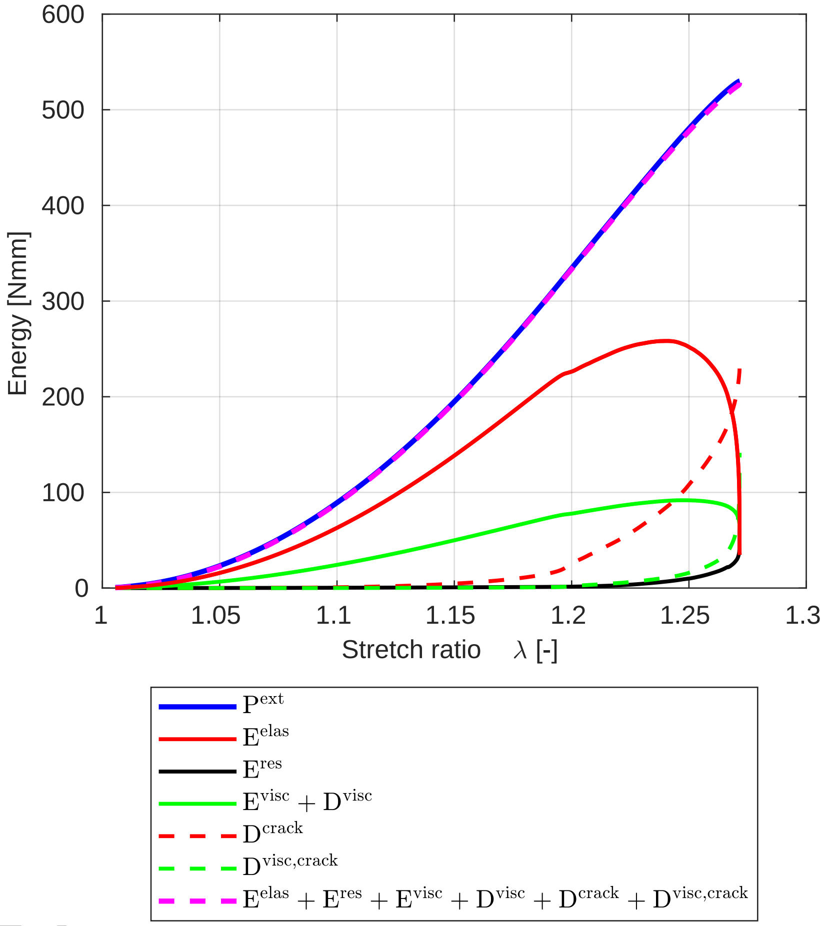

Figure 4.13: SENT test 200mm/min: Energy of the system

4.7. Validation

In this subsection, we use the optimized set of material parameters (table 4.2) and perform additional validation tests with different geometries and loading rates.

4.7.1. Double-edge notch tensile test with variable initial crack length

First, we investigate the DENT test, as depicted in figure 4.1, and change the initial crack size. This experiment was first reported by [59] and later used by others ([1], [19],[20]) to validate damage models for rubber. We have repeated these experiments for our EPDM rubber with a crack size $z = [3mm; 5mm; 7mm; 9mm]$ and a clamp velocity of $75mm/min$. In figure 4.14 we present the measured and calculated force to stretch ratio response for all crack sizes. We observe a good agreement between the experimental data and computed predictions. Although the maximum stretch is slightly underestimated for all initial crack lengths, the maximum tearing force is accurately predicted.

4.7.2. Double-edge notch tensile test with variable loading rate

Next, we continue with an initial crack length of $z = 7mm$ and change the loading rate $[25 .. 200mm/min]$ for the DENT test (figure 4.15). The experimentally observed increase of the maximum tearing force is successfully captured by the proposed model.

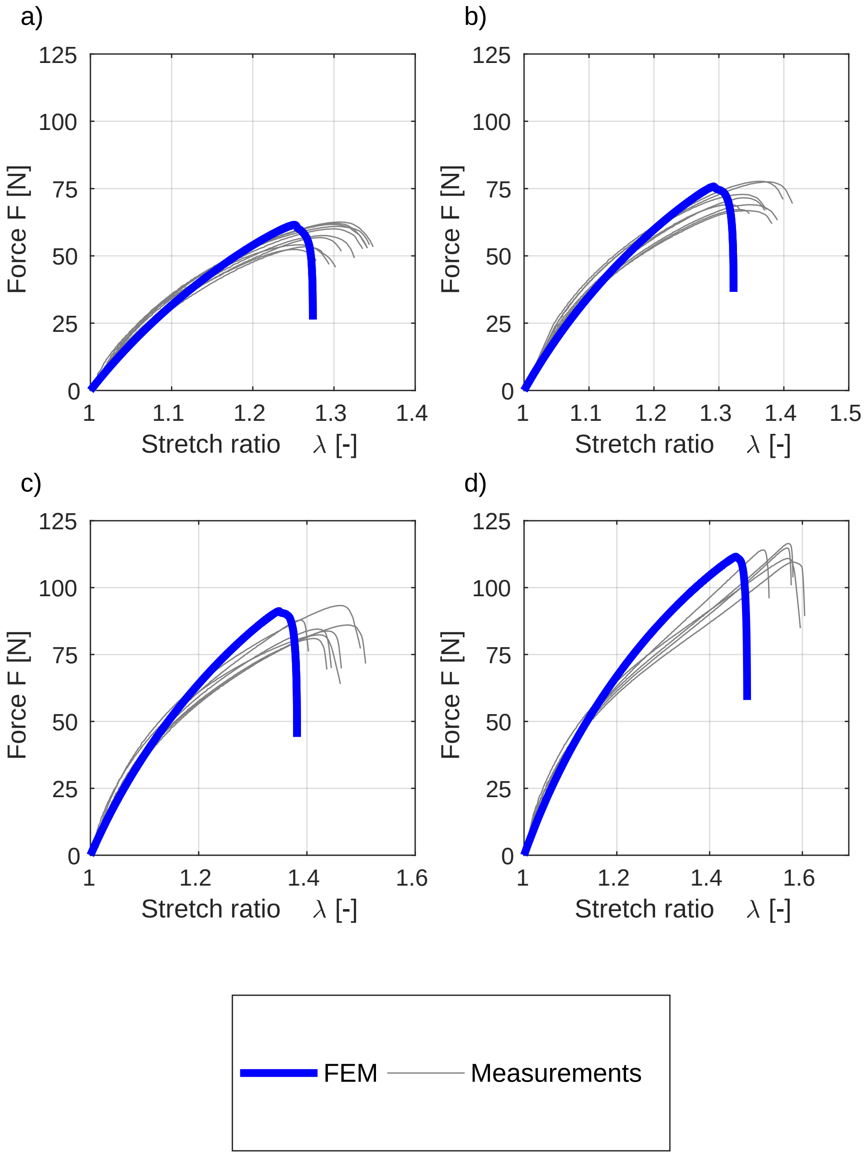

Figure 4.14: DENT test: Numerical and experimental force to stretch ratio response for a clamp velocity $75mm/min$. a) Initial crack length $z = 9mm$ b) Initial crack length $z = 7mm$ c) Initial crack length $z = 5mm$, d) Initial crack length $z = 3mm$.

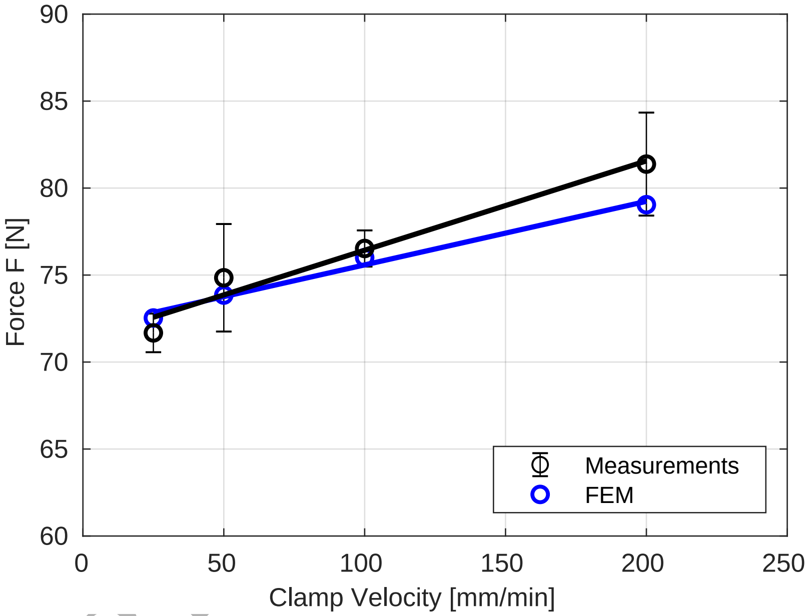

Figure 4.15: DENT tests: Numerically predicted and experimentally observed maximum tearing force (initial crack length $z = 7mm$) for different loading rates.

4.7.3. Multi-notch tensile test

The last geometrical set up includes three initial cracks (see figure 4.16), which coalesce during elongation. This example highlights the capabilities of the phase-field damage method to track complex crack patterns. Comparing figures 4.16 a) and b), we see that the numerical predicted crack path matches with the one observed in the experiment. Furthermore, we see in figure 4.17 an acceptable match of the experimental force to stretch ratio responses.

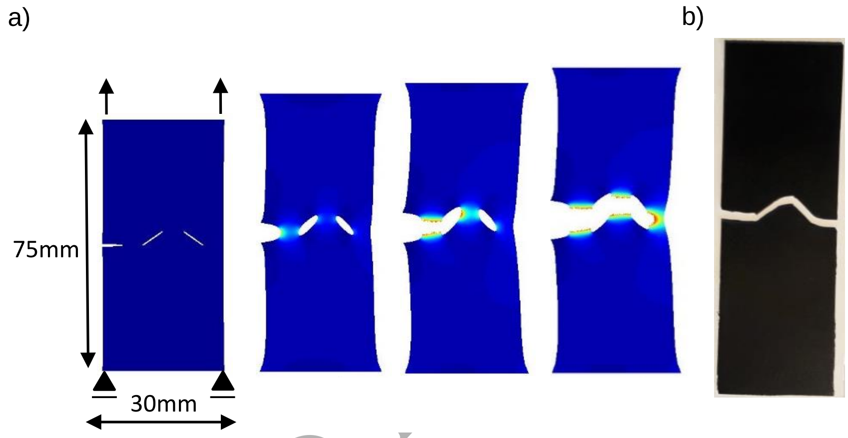

Figure 4.16: Multi notch tensile test: a) Numerically predicted crack path. b) Crack in the experiment.

4.7.4. Double-edge notch creep tensile test

Non-crystallizing rubbers such as EPDM show continuous crack growth under static loading. We conduct a double-edge notch tension creep test (initial crack length $z = 7mm$). A force of $65N$ is applied (clamp velocity $100mm/min$) leading to a displacement $u_{y,65N}$ at time $t = 0s$. The model, as can be seen in figure 4.18, predicts the time to failure accurately.

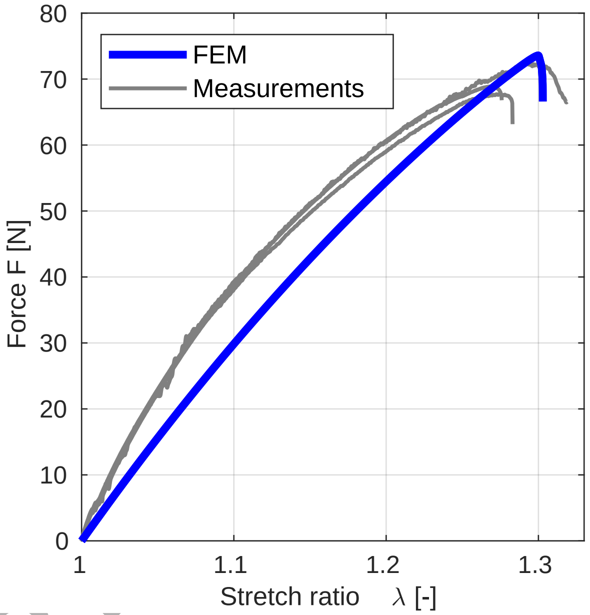

Figure 4.17: Multi notch tensile test: Numerically predicted and experimentally measured force to stretch ratio response, clamp velocity: $25mm/min$.

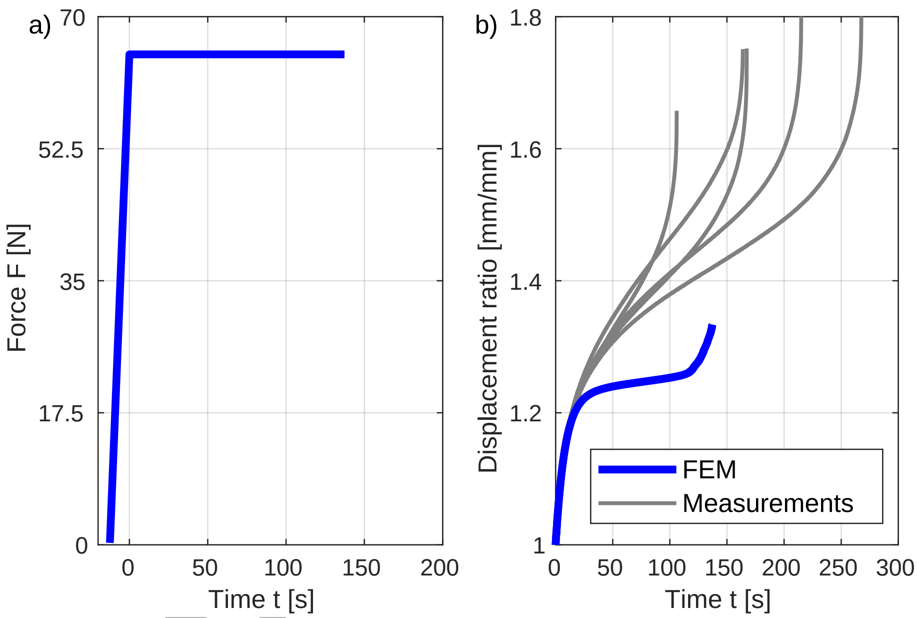

Figure 4.18: DENT creep test: a) Applied force over time b) Numerically predicted and experimentally measured displacement ratio $\frac{u_y}{u_{y,65N}}$ over time for a constant force of $65N$.

5. Concluding remarks

A rate-dependent phase-field damage model is introduced. We have included the rate-dependency in the damage formulation as well as in the constitutive behavior of the bulk. The bulk response is modeled with a reduced polynomial hyperelastic material model with three parameters [36] and the bulk's viscosity is incorporated according to [37]. The material parameters for the bulk are calibrated with uniaxial tensile tests, while the fracture parameters are obtained from single and double-edge tensile tests with different clamp velocities. Capturing local strains near the crack tip with digital image correlation has allowed us to identify the length scale parameter. We have also assessed three different degradation functions and have observed that the quadratic one fits the experimental data best. The presented validation cases, which are true predictions, have shown amongst others that the model is capable to accurately predict the time to failure for a creep test. Future work may extend the model to incorporate temperature dependency and fatigue damage.

Appendix A. Results degradation function $g_{d,2}$ and $g_{d,3}$

In this appendix, we present the results for of the SENT test with an initial crack length $z = 20mm$, as depicted in figure 4.1a), for a loading rate of $25mm/min$ and $200mm/min$. Subsequently, the results of the DENT test (figure 4.1b) for clamp velocity $75mm/min$ and varying crack size $z = [3mm; 5mm; 7mm; 9mm]$ are plotted, as well as the results for the DENT test with fixed crack length $z = 7mm$ and varying clamp velocity. At first, we show the result for the degradation function $g_{d,2}$ (figure A.1, A.2 and A.3), then the results for degradation function $g_{d,3}$ (figure A.4, A.5 and A.6).

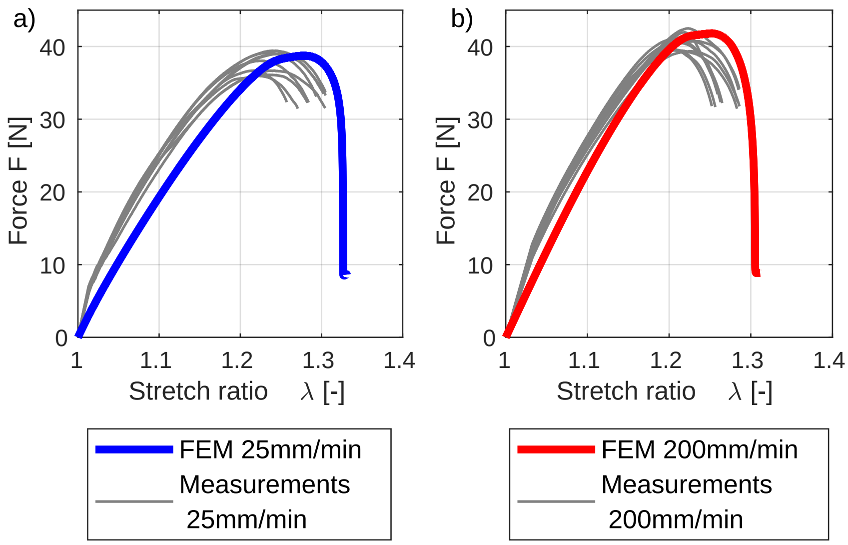

Figure A.1: SENT test for degradation function $g_{d,2}$: Numerical and experimental results a) Force to stretch-ratio response for $25mm/min$. b) Force to stretch-ratio response for $200mm/min$.

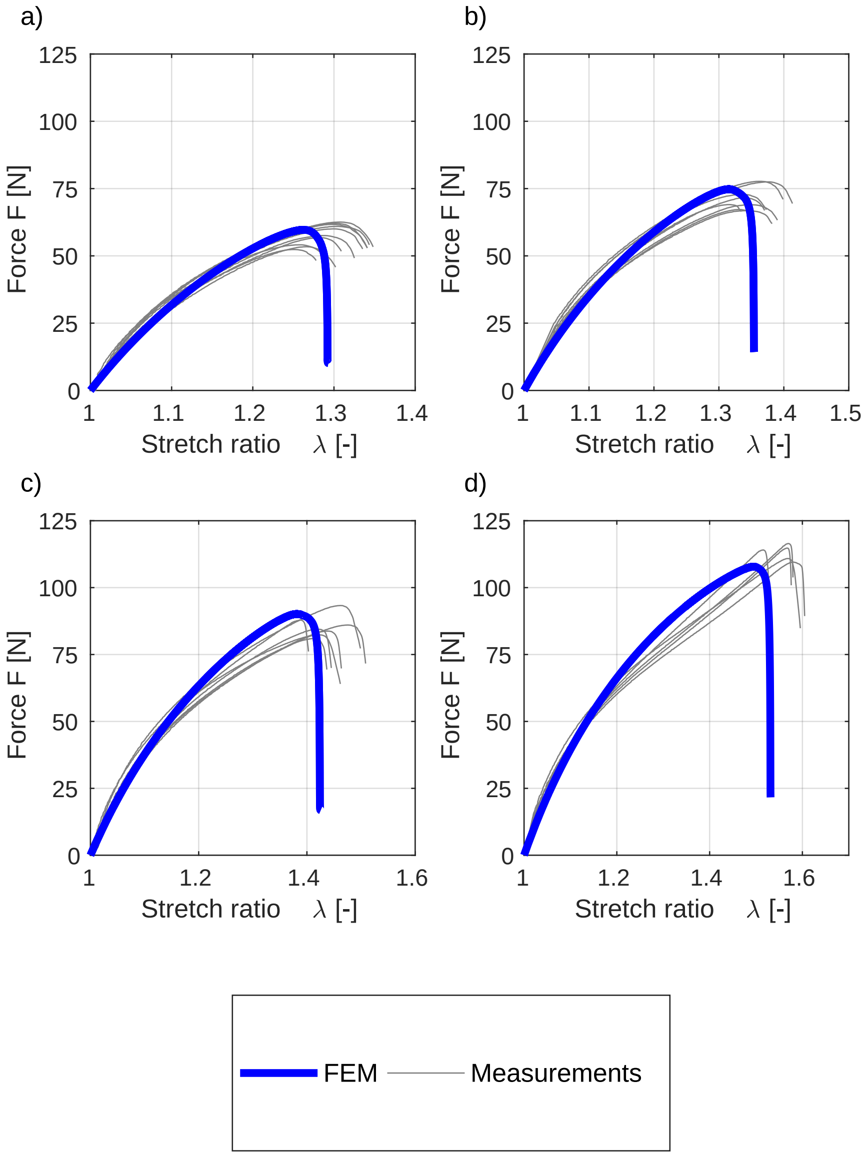

Figure A.2: DENT test for degradation function $g_{d,2}$: Numerical and experimental force to stretch ratio response for a clamp velocity $75mm/min$. a) Initial crack length $z = 9mm$ b) Initial crack length $z = 7mm$ c) Initial crack length $z = 5mm$, d) Initial crack length $z = 3mm$.

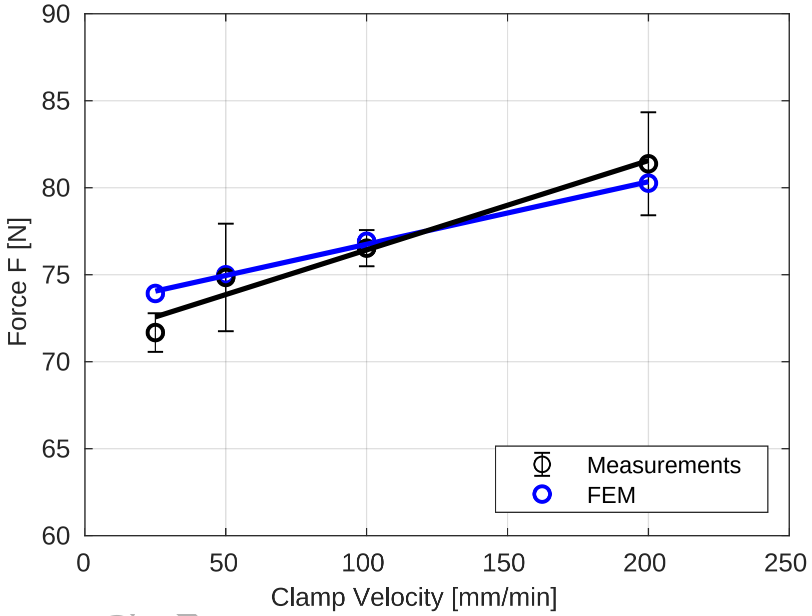

Figure A.3: DENT tests for degradation function $g_{d,2}$: Numerically predicted and experimentally observed maximum tearing force (initial crack length $z = 7mm$) for different loading rates.

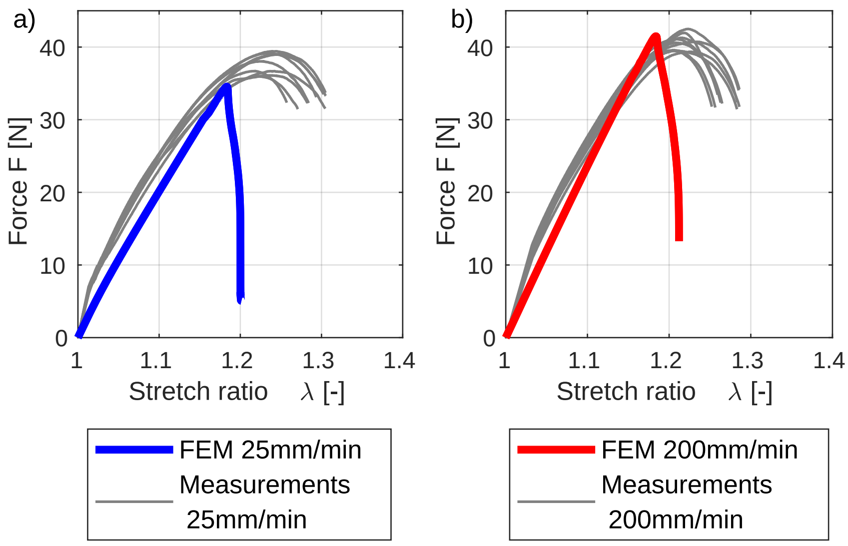

Figure A.4: SENT test for degradation function $g_{d,3}$: Numerical and experimental results a) Force to stretch-ratio response for $25mm/min$. b) Force to stretch-ratio response for $200mm/min$.

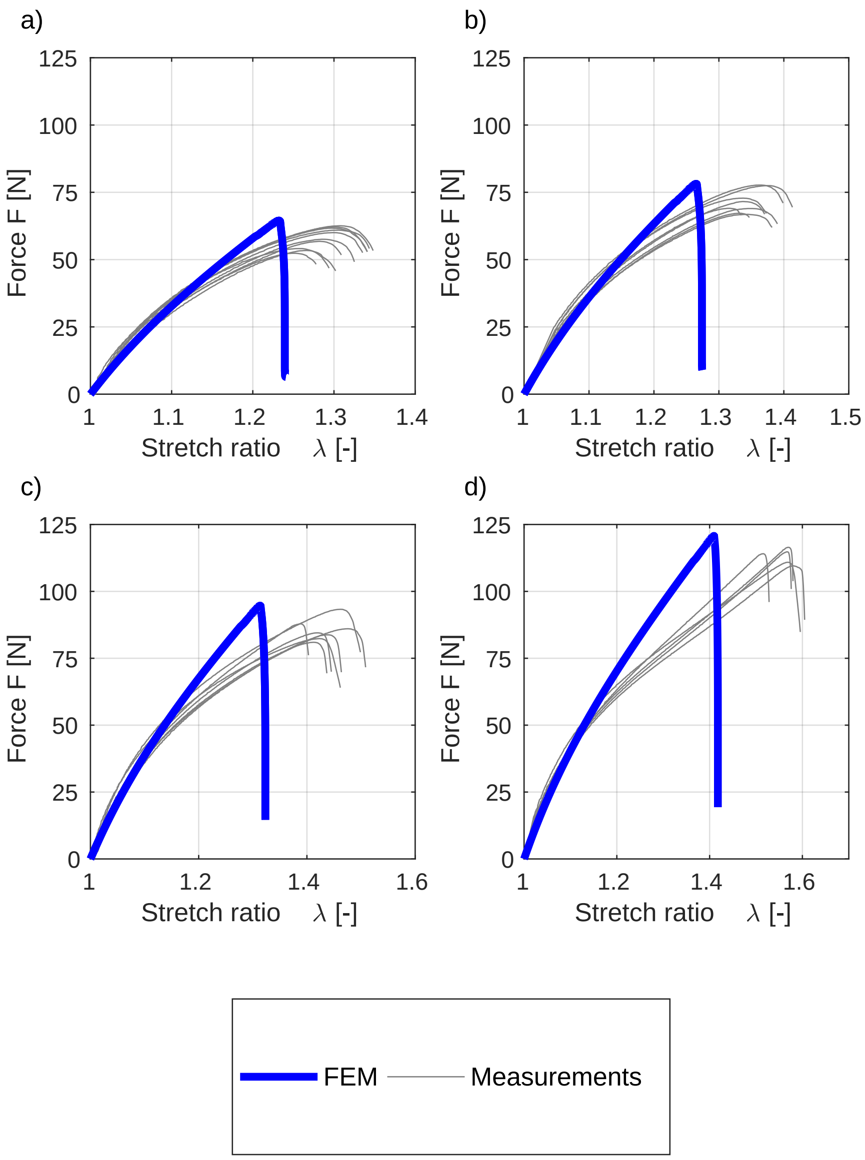

Figure A.5: DENT test for degradation function $g_{d,3}$: Numerical and experimental force to stretch ratio response for a clamp velocity $75mm/min$. a) Initial crack length $z = 9mm$ b) Initial crack length $z = 7mm$ c) Initial crack length $z = 5mm$, d) Initial crack length $z = 3mm$.

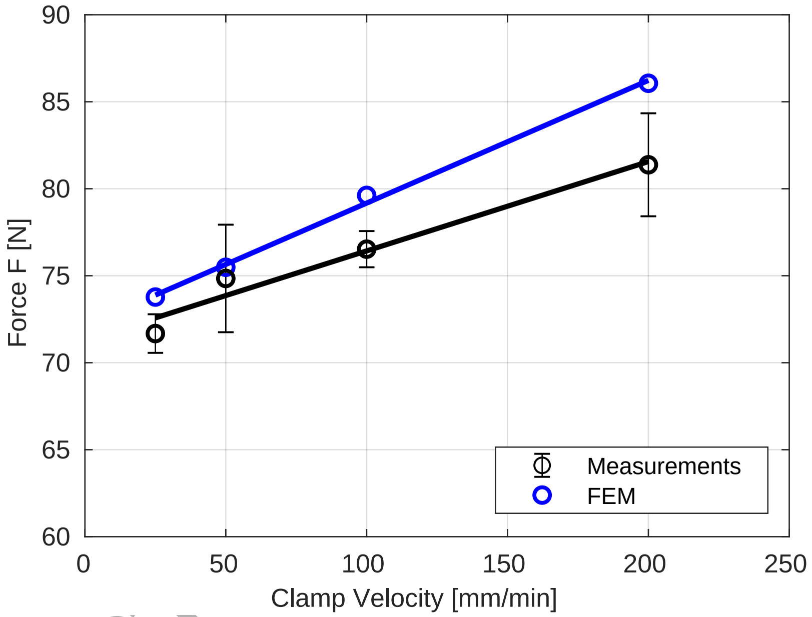

Figure A.6: DENT tests for degradation function $g_{d,3}$: Numerically predicted and experimentally observed maximum tearing force (initial crack length $z = 7mm$) for different loading rates.

References

[1] C. Miehe and L.-M. Schänzel. Phase field modeling of fracture in rubbery polymers. Part I: Finite elasticity coupled with brittle failure. *Journal of the Mechanics and Physics of Solids*, 65:93–113, 2014.

[2] A. Kumar, G. A. Francfort, and O. Lopez-Pamies. Fracture and healing of elastomers: A phase-transition theory and numerical implementation. *Journal of the Mechanics and Physics of Solids*, 2018.

[3] B. Talamini, Y. Mao, and L. Anand. Progressive damage and rupture in polymers. *Journal of the Mechanics and Physics of Solids*, 111(2012):434–457, 2018.

[4] P. B. Lindley. Non-Relaxing Crack Growth and Fatigue in a Non-Crystallizing Rubber. *Rubber Chemistry and Technology*, 47(5):1253–1264, 1974.

[5] G. J. Lake. Fatigue and Fracture of Elastomers. *Rubber Chemistry and Technology*, 68(3):435–460, 1995.

[6] A. G. Thomas. The Developement of Fracture Mechanics for Elastomers. *Rubber Chemistry and Technology*, 67:50–60, 1994.

[7] K. Özenc and M. Kaliske. An implicit adaptive node-splitting algorithm to assess the failure mechanism of inelastic elastomeric continua. *International Journal for Numerical Methods in Engineering*, 100:669–688, 2014.

[8] E. Elmukashfi and M. Kroon. Numerical analysis of dynamic crack propagation in biaxially strained rubber sheets. *Engineering Fracture Mechanics*, 124-125:1–17, 2014.

[9] C. Miehe, M. Hofacker, and F. Welschinger. A phase field model for rate-independent crack propagation: Robust algorithmic implementation based on operator splits. *Computer Methods in Applied Mechanics and Engineering*, 199(45-48):2765–2778, 2010.

[10] B. Bourdin, G. A. Francfort, and J. J. Marigo. Numerical experiments in revisited brittle fracture. *Journal of the Mechanics and Physics of Solids*, 48(4):797–826, 2000.

[11] R. H. J. Peerlings, R. de Borst, W. A. M. Brekelmans, and J. H. P. de Vree. Gradient enhanced damage for quasi-brittle materials. *International Journal for Numerical Methods in Engineering*, 39(19):3391–3403, 1996.

[12] L. H. Poh and G. Sun. Localizing gradient damage model with decreasing interactions. *International Journal for Numerical Methods in Engineering*, 110(6):503–522, 2017.

[13] K. Pham, H. Amor, J.-J. J. Marigo, and C. Maurini. Gradient damage models and their use to approximate brittle fracture. *International Journal of Damage Mechanics*, 20(4):618–652, 2011.

[14] G. Sun and L. H. Poh. Homogenization of intergranular fracture towards a transient gradient damage model. *Journal of the Mechanics and Physics of Solids*, 95:374–392, 2016.

[15] Z. Wang and L. H. Poh. A homogenized localizing gradient damage model with micro inertia effect. *Journal of the Mechanics and Physics of Solids*, 116:370–390, 2018.

[16] R. de Borst and C. V. Verhoosel. Gradient damage vs phase-field approaches for fracture: Similarities and differences. *Computer Methods in Applied Mechanics and Engineering*, 2016.

[17] C. Steinke, I. Zreid, and M. Kaliske. On the relation between phase-field crack approximation and gradient damage modelling. *Computational Mechanics*, 59(5):717–735, 2017.

[18] A. Raina and C. Miehe. A phase-field model for fracture in biological tissues. *Biomechanics and Modeling in Mechanobiology*, 15(3):1–18, 2015.

[19] O. Gueltekin, H. Dal, and G. A. Holzapfel. A phase-field approach to model fracture of arterial walls: Theory and finite element analysis. *Computer Methods in Applied Mechanics and Engineering*, 2016.

[20] J. Wu, C. McAuliffe, H. Waisman, and G. Deodatis. Stochastic analysis of polymer composites rupture at large deformations modeled by a phase field method. *Computer Methods in Applied Mechanics and Engineering*, 2016.

[21] B. San and H. Waisman. Optimization of Carbon Black Polymer Composite Microstructure for Rupture Resistance. *Journal of Applied Mechanics*, 84(2):021005, 2016.

[22] O. Gültekin, H. Dal, and G. A. Holzapfel. Numerical aspects of anisotropic failure in soft biological tissues favor energy-based criteria: A rate-dependent anisotropic crack phase-field model. *Computer Methods in Applied Mechanics and Engineering*, 331:23–52, 2018.

[23] X. Zhang, C. Vignes, S. W. Sloan, and D. Sheng. Numerical evaluation of the phase-field model for brittle fracture with emphasis on the length scale. *Computational Mechanics*, pages 1–16, 2017.

[24] T. T. Nguyen, J. Yvonnet, M. Bornert, C. Chateau, K. Sab, R. Romani, and R. Le Roy. On the choice of parameters in the phase field method for simulating crack initiation with experimental validation. *International Journal of Fracture*, 197(2):213–226, 2016.

[25] F. Freddi and G. Royer-Carfagni. Regularized variational theories of fracture: A unified approach. *Journal of the Mechanics and Physics of Solids*, 58(8):1154–1174, 2010.

[26] G. Del Piero. A variational approach to fracture and other inelastic phenomena. *A Variational Approach to Fracture and Other Inelastic Phenomena*, 9789400772:1–80, 2014.

[27] E. Tanné, T. Li, B. Bourdin, J. J. Marigo, and C. Maurini. Crack nucleation in variational phase-field models of brittle fracture. *Journal of the Mechanics and Physics of Solids*, 110:80–99, 2018.

[28] K. H. Pham, K. Ravi-Chandar, and C. M. Landis. Experimental validation of a phase-field model for fracture. *International Journal of Fracture*, 205(1):83–101, 2017.

[29] M. G. D. Geers, R. de Borst, W. A.M. Brekelmans, and R. H. J. Peerlings. Validation and internal length scale determination for a gradient damage model: application to short glass-fibre-reinforced polypropylene. *International Journal of Solids and Structures*, 36(17):2557–2583, 1999.

[30] M. Klinsmann, D. Rosato, M. Kamlah, and R. M. McMeeking. An assessment of the phase field formulation for crack growth. *Computer Methods in Applied Mechanics and Engineering*, 294:313–330, 2015.

[31] M. J. Borden, T. J. R. Hughes, C. M. Landis, A. Anvari, and I. J. Lee. A phase-field formulation for fracture in ductile materials: Finite deformation balance law derivation, plastic degradation, and stress triaxiality effects. *Computer Methods in Applied Mechanics and Engineering*, 312:130–166, 2016.

[32] J. Bonet and R. D. Wood. *Nonlinear Continuum Mechanics for Finite Element Analysis*. Cambridge University Press, 2008.

[33] R. W. Penn. Volume Changes Accompanying the Extension of Rubber. *Journal of Rheology*, 14(1970):509, 1970.

[34] R. W. Ogden. Volume changes associated with the deformation of rubber-like solids. *Journal of the Mechanics and Physics of Solids*, 24(6):323–338, 1976.

[35] A. Ilseng, B. H. Skallerud, and A. H. Clausen. An experimental and numerical study on the volume change of particle-filled elastomers in various loading modes. *Mechanics of Materials*, 106:44–57, 2017.

[36] O. H. Yeoh. Some Forms of the Strain Energy Function for Rubber, 1993.

[37] G. A. Holzapfel. On large strain viscoelasticity: continuum formulation and finite element applications to elastomeric structures. *International Journal for Numerical Methods in Engineering*, 39(22):3903–3926, 1996.

[38] J. S. Bergström and M. C. Boyce. Constitutive modeling of the large strain time-dependent behavior of elastomers. *Journal of the Mechanics and Physics of Solids*, 46(5):931–954, 1998.

[39] G. Ayoub, F. Zaïri, M. Naït-Abdelaziz, J. M. Gloaguen, and G. Kridli. A visco-hyperelastic damage model for cyclic stress-softening, hysteresis and permanent set in rubber using the network alteration theory. *International Journal of Plasticity*, 54:19–33, 2014.

[40] S. Reese and S. Govindjee. A Theory of Finite Viscoelasticity and Numerical Aspects. *International Journal for Solids Structures*, 35(97), 1998.

[41] A. A. Griffith. *The Phenomena of Rupture and Flow in Solids*. Philosophical transactions / Royal Society of London. 1920.

[42] N. Moës, J. Dolbow, and T. Belytschko. A finite element method for crack growth without remeshing. *International Journal for Numerical Methods in Engineering*, 46(1):131–150, 1999.

[43] B. Bourdin, J. J. Marigo, C. Maurini, and P. Sicsic. Morphogenesis and propagation of complex cracks induced by thermal shocks. *Physical Review Letters*, 112(1):1–5, 2014.

[44] H. Amor, J. J. Marigo, and C. Maurini. Regularized formulation of the variational brittle fracture with unilateral contact: Numerical experiments. *Journal of the Mechanics and Physics of Solids*, 57(8):1209–1229, 2009.

[45] C. Miehe, F. Welschinger, and M. Hofacker. Thermodynamically consistent phase-fieldmodels of fracture: Variational principles and multi-field

FE implementations. *International Journal for Numerical Methods in Engineering*, 83(10):1273–1311, 2010.

[46] N. Singh, C. V. Verhoosel, R. De Borst, and E. H. Van Brummelen. A fracture-controlled path-following technique for phase-field modeling of brittle fracture. *Finite Elements in Analysis and Design*, 113:14–29, 2016.

[47] S. Wright and J. Nocedal. Numerical optimization. *Springer Science*, 35(67-68):7, 1999.

[48] P. Shanthraj, L. Sharma, B. Svendsen, F. Roters, and D. Raabe. A phase field model for damage in elasto-viscoplastic materials. *Computer Methods in Applied Mechanics and Engineering*, 312:167–185, 2016.

[49] Correlate. *version 2017*. GOM GmbH, Braunschweig, Germany, 2018.

[50] MATLAB. *version R2018a*. The MathWorks Inc., Natick, Massachusetts, 2018.

[51] H. Rappel, L. A. A. Beex, and S. P. A. Bordas. Bayesian inference to identify parameters in viscoelasticity. *Mechanics of Time-Dependent Materials*, 22(2):221–258, 2018.

[52] J.-Y. Wu and P. V. Nguyen. A length scale insensitive phase-field damage model for brittle fracture. *Journal of the Mechanics and Physics of Solids*, 119(l):20–42, 2018.

[53] E. M. Arruda and M. C. Boyce. A Three-dimensional Constitutive Model for the Large Stretch Behaviour of Rubber Elastic Materials. *Journal of Mechanics and Physics of Solids*, 41(2):389–412, 1993.

[54] J. M. Sargado, E. Keilegavlen, I. Berre, and J. M. Nordbotten. High-accuracy phase-field models for brittle fracture based on a new family of degradation functions. *Journal of the Mechanics and Physics of Solids*, 111:458–489, 2018.

[55] C. Kuhn, A. Schlüter, and R. Müller. On degradation functions in phase field fracture models. *Computational Materials Science*, 108:374–384, 2015.

[56] K. Y. Volokh. Characteristic Length of Damage Localization in Rubber. *International Journal of Fracture*, 168(1):113–116, 2011.

[57] J. R. Samaca Martinez, E. Toussaint, X. Balandraud, J. B. Le Cam, and D. Berghezan. Heat and strain measurements at the crack tip of filled rubber under cyclic loadings using full-field techniques. *Mechanics of Materials*, 81:62–71, 2015.

[58] H. Zhang, A. K. Scholz, J. De Crevoisier, D. Berghezan, T. Narayanan, E. J. Kramer, and C. Creton. Nanocavitation around a crack tip in a soft nanocomposite: A scanning microbeam small angle X-ray scattering study. *Journal of Polymer Science, Part B: Polymer Physics*, 53(6):422–429, 2015.

[59] N. A. Hocine, M. N. Abdelaziz, and A. Imad. Fracture problems of rubbers: J-integral estimation based upon η factors and an investigation on the strain energy density distribution as a local criterion. *International Journal of Fracture*, 117(1):1–23, 2002.